

# Lithospheric models supported by the Caribbean and Levant examples help rethink transpression at plate boundaries

Received: 9 July 2025

Accepted: 16 December 2025

Published online: 06 January 2026

 Check for updates

Anthony Jourdon<sup>1,2</sup>✉, Laetitia Le Pourhiet<sup>1,3</sup>, Dave A. May<sup>4</sup>,  
Manuel Pubellier<sup>5</sup> & Alice-Agnes Gabriel<sup>4,6</sup>

Strike-slip restraining bends, such as the Levant Fault, belonging to push-up systems and the Jamaican fault network, belonging to duplex systems, display a diversity of fault geometries and deformation patterns that reflect distinct modes of lithospheric-scale strain localization. To investigate the origin of this variability, we develop 3D numerical models of transpressional strike-slip systems using heterogeneous simple shear boundary conditions and thermally-dependent, non-linear rheology. Unlike classical analog or numerical models that impose velocity discontinuities, our approach allows spontaneous fault localization that naturally generates transpression. We systematically explore how the position and geometry of inherited weak zones influence fault development. We show that three distinct strike-slip systems emerge: (1) push-up systems with a single strike-slip fault and outward-propagating thrusts; (2) duplex systems with interacting parallel faults connected by P-shears; and (3) systems of non-interacting parallel faults. These results highlight spontaneous strike-slip localization and how initial heterogeneities control formation and evolution of long-term lithospheric deformation.

Strike-slip deformation occurs across a wide range of scales, from tens of meters to thousands of kilometers, including features from outcrop-scale faults to plate boundaries<sup>1–3</sup>. Strike-slip systems consist of individual fault segments that either connect directly to a principal fault through hard-links or distribute into deformation zones where faults do not directly connect, forming soft-links. These segments often organize into relays, which can be either transpressional or transtensional, depending on the geometry of the step-over and the sense of slip<sup>4</sup>. Transtensional relays are generally associated with releasing bends and pull-apart basins [e.g.,<sup>5–7</sup>], where the crust or lithosphere undergoes thinning. In contrast, transpressional relays are linked to restraining bends, which promote crustal and/or lithospheric thickening. In nature, restraining bends fall into two main structural categories<sup>8–11</sup>: duplex systems (Fig. 1a) characterized by parallel,

lithospheric-scale strike-slip faults linked by oblique transpressive shear zones accommodating shortening and push-up systems, characterized by two offset strike-slip fault segments describing a step-over connected by a sigmoidal transpressive structure and surrounded by thrusts propagating outward from the strike-slip faults system (Fig. 1b). A third configuration can occur when the spacing between strike-slip segments is large enough that they interact only weakly, resulting in subparallel fault arrays with limited deformation in between. Duplex systems are observed at diffuse transpressive plate boundaries such as the northern California Shear Zone<sup>12</sup>, the northern Caribbean plate boundary<sup>13</sup>, or the Chaman plate boundary<sup>14</sup>, while lithospheric-scale examples of push-up structures include the Arabia-Africa plate boundary in the Lebanon and Anti-Lebanon mountains along the Levant Fault system<sup>15</sup>, and the Sorong Fault in the Bird's Head

<sup>1</sup>Sorbonne Université, CNRS, IStEP, Institut des Sciences de la Terre de Paris, UMR7193, Paris, France. <sup>2</sup>Université Côte d'Azur, Observatoire de la Côte d'Azur, CNRS, IRD, Géoazur, Valbonne, France. <sup>3</sup>Institut Universitaire de France, Paris, France. <sup>4</sup>Institute of Geophysics and Planetary Physics, Scripps Institution of Oceanography, UC San Diego, La Jolla, CA, USA. <sup>5</sup>Laboratoire de Géologie, UMR8538, CNRS, École Normale Supérieure, Paris, France. <sup>6</sup>Department of Earth and Environmental Sciences, Ludwig-Maximilians-Universität München, Munich, Germany. ✉e-mail: [anthony.jourdon@geoazur.unice.fr](mailto:anthony.jourdon@geoazur.unice.fr)

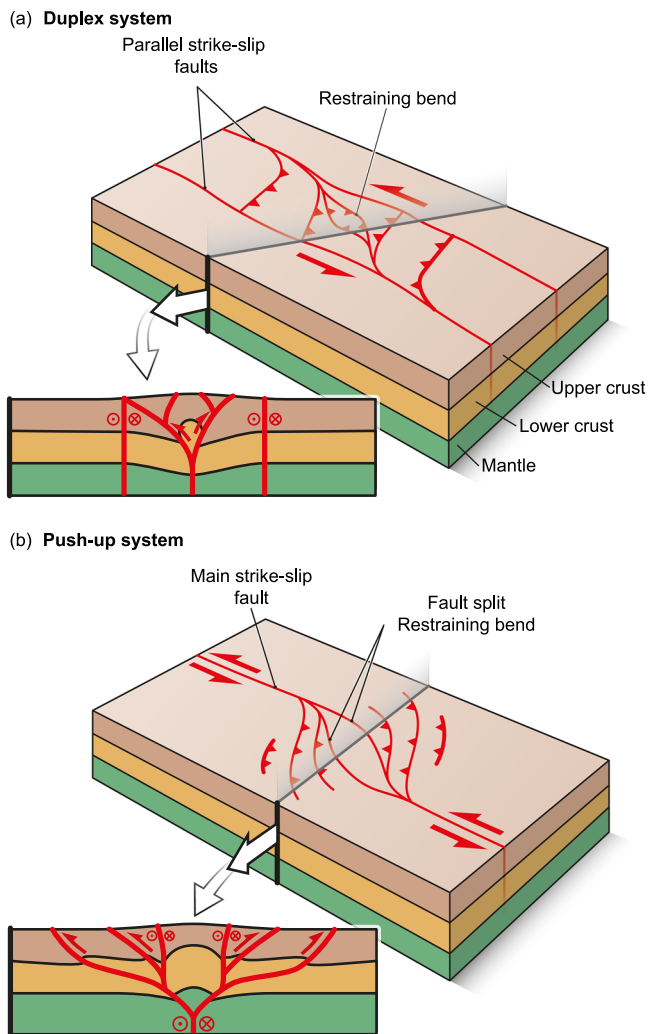


**Fig. 1 | Schematic representation of natural restraining bends. a** Duplex system, where parallel strike-slip faults link with a restraining bend as in Jamaica<sup>4</sup>. **b** Push-up system, where a single strike-slip fault splits at shallow depth into two sigmoidal-shaped segments forming a restraining bend as along the Levant Fault in Lebanon [e.g., ref. 97. At depth, the two segments connect to a single strike-slip fault through a hard-link.

Peninsula in northwest New Guinea<sup>16</sup> resulting from strain partitioning in the Australian plate.

Although these structures and their kinematics are well documented in nature, their underlying dynamics remain challenging to reproduce in models. Push-up systems have been extensively investigated in numerical and analog experiments<sup>17–27</sup>, but models of lithospheric-scale networks of strike-slip faults [e.g., refs. 28–30] or more specifically, duplex systems are more rarely modeled<sup>31,32</sup>.

A key challenge arises from how boundary conditions are imposed. Classic Riedel experiments prescribe basal velocity discontinuities, assuming the existence of one or several pre-localized shear zones at depth [e.g., refs. 1,17,33–39] that can be combined with imposed fault geometries [e.g., refs. 19,20,25–27,40] to generate restraining and releasing bends. While well-suited for studying deformation in sedimentary basins above known basement faults, this approach does not capture the strain localization processes that initiate the formation of lithospheric-scale strike-slip zones. Lateral indenter-type models [e.g., refs. 41–45] provide an alternative, but rely on step or arctangent velocity functions imposed at the boundaries of the system, which still constrains localization externally rather than

allowing it to emerge. Other numerical studies have employed periodic boundary conditions [e.g., refs. 46,47] enforcing symmetry in the system or stress-free boundary conditions [e.g., ref. 21] neglecting the resistance of surrounding lithosphere and thus limiting their applicability to various systems at the plate-boundary scale.

In natural systems, however, deformation often localizes progressively within heterogeneous lithosphere that can be influenced by pre-existing structures such as lithological contacts and inherited faults<sup>48–51</sup>. Fault patterns may also be controlled by rheological layering, ductile shear zones and the depth-dependent mechanics of strain localization in the lithosphere, as suggested by observations of conjugate fault sets like those activated during the 2019 Ridgecrest earthquake<sup>52–54</sup>. Capturing this self-consistent evolution in models requires approaches that avoid prescribing discontinuities or arbitrary velocity variations across fault zones.

Here, we employ a 3D numerical framework<sup>55</sup> that enables the spontaneous development of lithospheric-scale strike-slip shear zones under simple shear boundary conditions, without imposing pre-existing faults or velocity discontinuities. Using this approach, we investigate the formation and evolution of restraining bends, and explore the conditions leading to push-up systems, duplex systems, or parallel fault systems. We then compare our numerical results with analog experiments and natural examples, focusing on the Levant Fault and the Jamaican fault network.

## Results

In the following results section, we refer to the fault orientation using the Riedel terminology<sup>6,56,57</sup> to ease the comparison between our models and the literature. The terminology distinguishes shear zones based on their orientation relative to the principal shear direction and their sense of shearing. The principal shear zone, denoted as Y-shear, is parallel to the regional simple shear direction and in the same sense of shearing (in our case left-lateral). The P-shear zones are oblique to the principal shear direction, oriented at an angle of approximately  $10\text{--}20^\circ$  ( $\phi/2$  where  $\phi$  is the friction angle of the material, clockwise and in the same sense of shearing). The R-shear zones are also oblique to the principal shear direction, oriented at an angle of approximately  $10\text{--}20^\circ$  counter-clockwise and in the same sense of shearing (right-lateral in our case). The R'-shear zones are oblique to the principal shear direction, oriented at an angle of approximately  $70\text{--}80^\circ$  counter-clockwise ( $\pi/2 - \phi/2$ ) but in the opposite sense of shearing (right-lateral in our case). Finally, the X-shear zones are oblique to the principal shear direction, oriented at an angle of approximately  $70\text{--}80^\circ$  clockwise and in the opposite sense of shearing too. We provide a diagram of these orientations in map view on Figs. 3, 5, and 7. We parameterize the initial geometry using the angle  $\alpha$  and the distance  $\Delta$  between two weak zones (Fig. 2c), to run 10 simulations. Initial weak zones are conceptualized as pre-existing lithospheric weaknesses, such as inherited structures or lithological contacts. However, their role is strictly to initiate deformation. While weak zones can be imposed as local cubes [e.g., refs. 58–60] or wide zones [e.g., refs. 61,62], we choose Gaussian distributions to avoid imposing arbitrary strain localization directions or mimicking specific geological features.

We find that the models first fall into two groups: those that form restraining bends and develop interactions, and those that do not. Then, among the models that form restraining bends, we identify two more groups based on the geometry of the strike-slip fault network and their time evolution. Therefore, we classify the models into three categories: push-up structures and duplex structures that belong to the group forming restraining bends, and parallel shear zones that belong to the group where no or poor interaction occurs (Fig. 3).

The push-up structure category in Fig. 3, encompasses models for which  $\alpha < 15^\circ$  such as models with  $\alpha = 7^\circ$ ,  $\Delta = 52$  km (Figs. 4, 5, Supplementary Figs. 1–3, Supplementary Movie 1),  $\alpha = 11^\circ$ ,  $\Delta = 65$  km (Supplementary Figs. 4–6, Supplementary Movie 2) and  $\alpha = 12.5^\circ$ ,

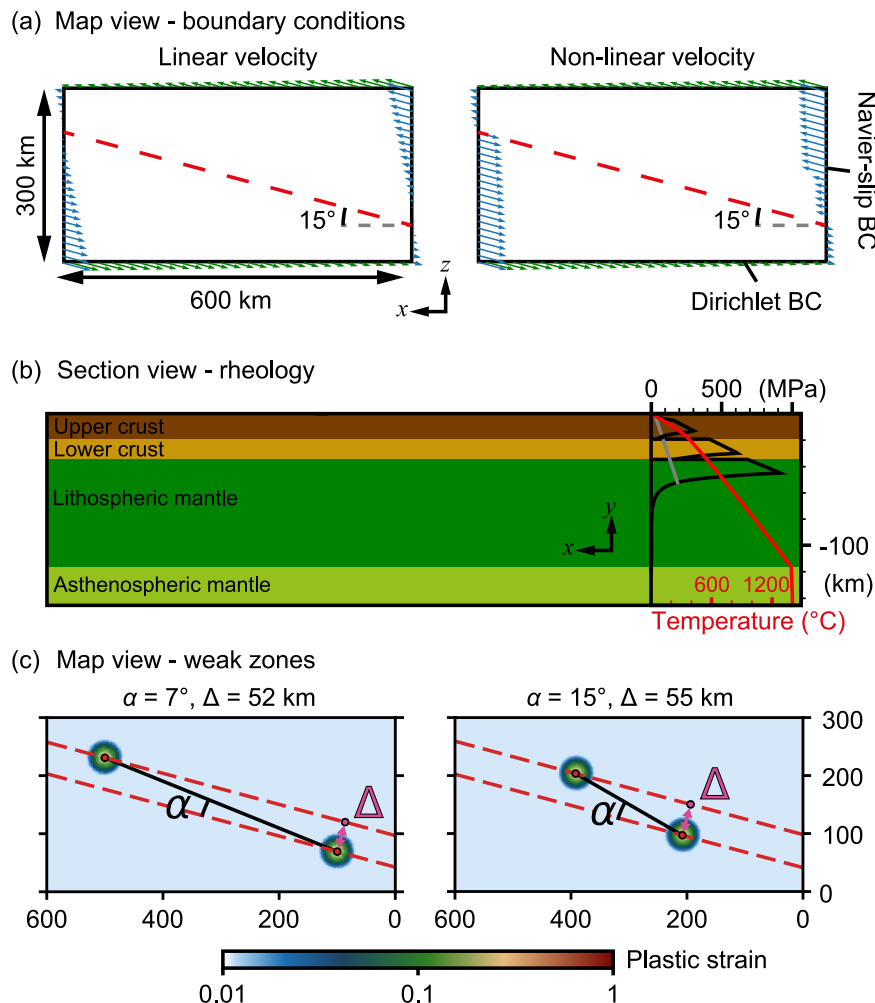


**Fig. 2 | Numerical models setup.** **a** Map view: domain geometry and boundary conditions. The red dashed line indicates the imposed shear direction. The green arrows indicate the imposed velocity, while the blue arrows exemplify the two end-member velocity fields resulting from the application of Navier-Slip condition when the strain rate is distributed (left) or localized (right) in the solution of the Stokes equation. **b** Vertical cross-section showing the initial rheological stratification. The

initial geotherm is in red. The initial yield stress envelope is in black. The grey curve shows the yield stress for the fully softened material at initial conditions. **c** Map view: initial plastic strain distribution. The red dashed lines indicate the shear direction passing by the centers of the two Gaussian functions.  $\alpha$  is the angle between the shear direction and the weak zones, and  $\Delta$  is the distance taken perpendicularly to the shear direction between the two weak zones.

$\Delta = 100$  km (Supplementary Figs. 7–9, Supplementary Movie 3). In these experiments, a principal strike-slip shear zone develops to form a restraining bend evolving into a push-up structure of different obliquities. Within the central region of the bend, deformation is characterized by transtension and extension, while compressional shear zones develop around the bend, resulting in a sigmoidal shape structure (Fig. 3).

The duplex structure category in Fig. 3, comprises models for which  $\alpha \geq 15^\circ$  and  $\Delta < 60$  km. For this category, we utilize the following combinations of  $\alpha$  and  $\Delta$ :  $\alpha = 15^\circ$ ,  $\Delta = 55$  km (Figs. 6, 7, Supplementary Figs. 10–12, Supplementary Movie 4),  $\alpha = 18^\circ$ ,  $\Delta = 50$  km (Supplementary Figs. 13–15, Supplementary Movie 5), and  $\alpha = 22.5^\circ$ ,  $\Delta = 50$  km (Supplementary Figs. 16–18, Supplementary Movie 6). These experiments result in the development of parallel Y-shear strike-slip zones connected by P-shear strike-slip zones. Compressional shear zones develop around these structures, creating a duplex strain pattern characterized by multiple main strike-slip shear zones running parallel to each other.

The parallel shear zones category in Fig. 3, includes models for which  $\alpha \geq 15^\circ$  and  $\Delta \geq 60$  km, such as models with  $\alpha = 15^\circ$ ,  $\Delta = 75$  km,  $\alpha = 17.5^\circ$ ,  $\Delta = 70$  km,  $\alpha = 17.5^\circ$ ,  $\Delta = 100$  km and  $\alpha = 20^\circ$ ,  $\Delta = 60$  km. These models also show parallel Y-shear strike-slip shear zones, but these

zones do not connect, resulting in minimal interaction. The outcome is a simple network of strike-slip faults parallel to each other that show limited deformation beyond the principal shear zones.

Among the ten experiments, we detail two cases representative of the push-up and duplex structure categories, respectively. The model using values of  $\alpha = 7^\circ$  and  $\Delta = 52$  km exemplifies the formation of sigmoidal push-up structures, whereas the model using values of  $\alpha = 15^\circ$  and  $\Delta = 55$  km demonstrates the development of duplex structures. Additional details about other models are provided in the supplementary data and supplementary movies. These models highlight the interaction between strike-slip shear zones in restraining bends and the emergence of compressional deformation patterns. In contrast, models producing parallel shear zones with limited interaction do not exhibit significant deformation beyond the principal shear zones and will not be further detailed.

#### Model $\alpha = 7^\circ$ , $\Delta = 52$ km

Figure 4 illustrates the evolution of the model with  $\alpha = 7^\circ$ ,  $\Delta = 52$  km. Initially, deformation localizes along the two weak zones, forming vertical strike-slip shear zones oriented parallel to the imposed simple shear direction. These shear zones propagate toward one another while accommodating a small portion of the total plate motion (2 cm

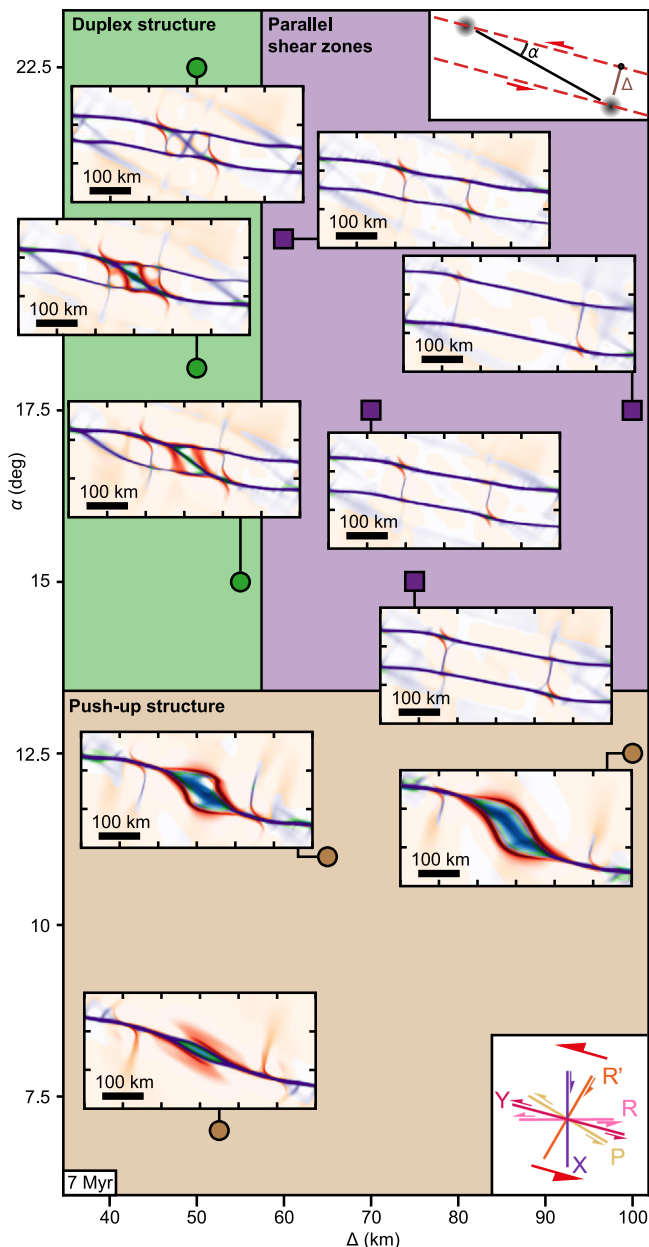


**Fig. 3 | Diagram summarizing the three categories of models based on the initial parameters  $\alpha$  and  $\Delta$ .** Pictures show the stress regime of the strain localization in models after 7 Myrs of evolution (See Figs. 4 & 6 for colors signification). The bottom right inset shows the orientation of the different shear zones in map view<sup>6,56,57</sup>.

$\text{yr}^{-1}$ ) with a slip rate of approximately  $-0.7 \text{ cm yr}^{-1}$ . At this stage, deformation remains diffuse, and topography is negligible.

By 4 Myrs, the shear zones link in the central region of the model via a P-shear, forming a restraining bend (Fig. 5). Positive topography begins to develop around this bend as deformation becomes more localized, and the slip rate on the fault increases to  $-1.4 \text{ cm yr}^{-1}$ .

At 6 Myrs, the strain localization varies with depth. In the lower crust and lithospheric mantle, deformation localizes on a single strike-slip shear zone. However, near the brittle-ductile transition, corresponding to the lower-upper crust interface, the central segment of the shear zone bifurcates into two branches. At the surface, transtensional deformation localizes between the two branches, while compressional shear zones develop both near the surface and at the brittle-ductile transition around the restraining bend.

By 8 Myrs, the spacing between the two branches increases, and the restraining bend evolves into a sigmoidal push-up structure. Right-lateral transpressional shear zones begin to localize at the edges of the restraining bend to accommodate rotations due to the reorientation of the main shear zone. Slip rates within the restraining bend vary, ranging from  $-1.65 \text{ cm yr}^{-1}$  at depth (single shear zone) to  $-1 \text{ cm yr}^{-1}$  at the surface (distributed across the two branches). High topography continues to develop, crustal thickening intensifies, and the lower crust begins to exhume. This exhumation forms a sigmoidal dome, with transtensional to extensional deformation localized above it.

At 12 Myrs, deformation propagates outward from the restraining bend, and well-localized thrust faults develop along each branch. The distribution of slip rates reflects this structural complexity:  $-1.7 \text{ cm yr}^{-1}$  at depth,  $-0.9 \text{ cm yr}^{-1}$  on the surface strike-slip branches, and  $-0.6 \text{ cm yr}^{-1}$  on the thrust faults. Additionally, right-lateral X-shear zones at the edges of the restraining bend accommodate rotation, with slip rates of  $-0.15 \text{ cm yr}^{-1}$ . Exhumation of the lower crust continues, carrying a slice of the lithospheric mantle between the two branches.

By 16 Myrs, the growing spacing between the two branches drives further outward deformation propagation. Thrust faults, initially parallel to the strike-slip shear zones, rotate to form an angle of  $-35^\circ$  with them, promoting the development of new, more external thrust faults, resulting in a rectangular shape structure. This reorientation is accompanied by a reduction in slip rates:  $-0.6 \text{ cm yr}^{-1}$  on the strike-slip branches and  $-0.4 \text{ cm yr}^{-1}$  on the thrust faults, while the deep strike-slip fault maintains a slip rate of  $-1.7 \text{ cm yr}^{-1}$ . A secondary family of thrust faults emerges near the right-lateral X-shear zones, accommodating additional shortening due to rotation.

#### Model $\alpha = 15^\circ$ , $\Delta = 55 \text{ km}$

Figure 6 illustrates the evolution of the model with  $\alpha = 15^\circ$ ,  $\Delta = 55 \text{ km}$ .

Initially, deformation localizes along two vertical left-lateral strike-slip shear zones oriented parallel to the imposed shear direction, exhibiting slip rates of approximately  $-0.7 \text{ cm yr}^{-1}$ . Conjugate right-lateral shear zones also develop, but their slip rates remain  $\leq 0.1 \text{ cm yr}^{-1}$ .

At 4 Myrs, the two left-lateral shear zones propagate parallel to each other and intersect the conjugate right-lateral shear zones, forming a rectangular geometry. At the external corners of this rectangle, compression due to fault interactions generates small thrusts and positive topography (Fig. 7). The slip rates on the northern shear zone increase to  $-0.9 \text{ cm yr}^{-1}$  in its central segment and  $-1.1 \text{ cm yr}^{-1}$  at its western extremity. The southern shear zone exhibits a slip rate of  $-0.8 \text{ cm yr}^{-1}$ , decreasing westward.

By 6 Myrs, two new P-shear zones begin to form, linking the parallel left-lateral shear zones. One develops at the western extremity of the southern shear zone, while the other forms in the central part of the rectangle. Slip rates continue to increase, reaching  $-1.3 \text{ cm yr}^{-1}$  on the northern shear zone and the newly forming central P-shear. Topography also builds at the junctions of the left- and right-lateral shear zones.

At 8 Myrs, the P-shear zones are fully localized, and restraining bends begin to form around them. The central P-shear zone, however, exhibits transtensional to extensional deformation in its central segment, while thrust faults develop around and root into the strike-slip shear zones, forming a positive flower structure, i.e., a crustal scale push-up visible in the topography (Fig. 7). Slip rates show notable variability across the system:  $-1.6 \text{ cm yr}^{-1}$  at the western junction of the shear zones, decreasing to  $-1.2 \text{ cm yr}^{-1}$  on the northern segment of the P-shear,  $-0.8 \text{ cm yr}^{-1}$  in its central portion, and  $-0.6 \text{ cm yr}^{-1}$  on the thrust faults.

By 12 Myrs, significant structural changes occur. A new left-lateral shear zone develops to the north, branching from the northernmost shear zone as a P-shear and evolving northwestward into a Y-shear,

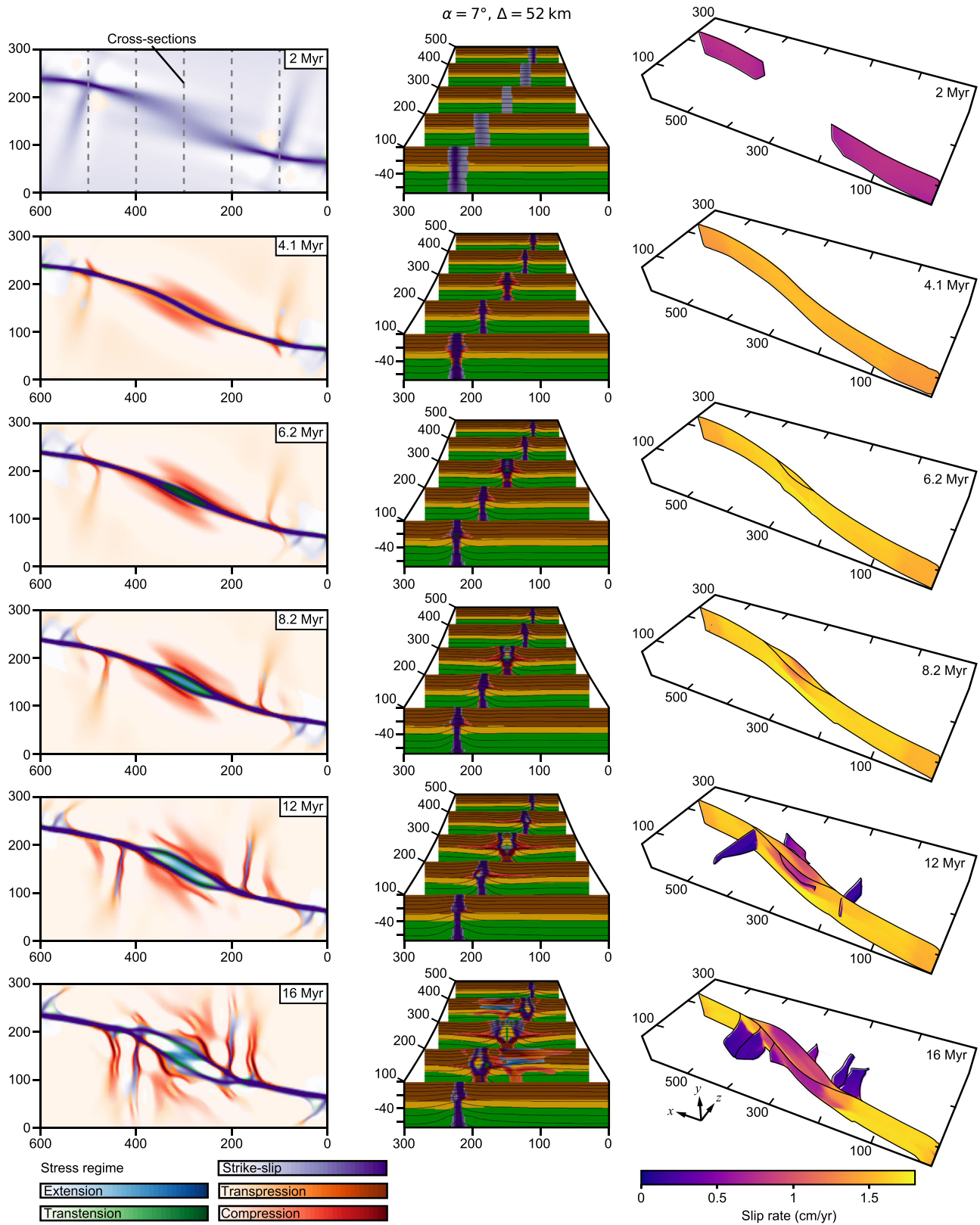


**Fig. 4 | Evolution of the model  $\alpha = 7^\circ, \Delta = 52 \text{ km}$ .** The left column shows the stress regime of the active deformation. The central column shows serial cross-sections with the stress regime superimposed. The right column shows the long-term slip

rate on the faults. Fault surfaces are reconstructed following ref. 108. Slip-rate estimation method is detailed in “Slip-rate estimation”.

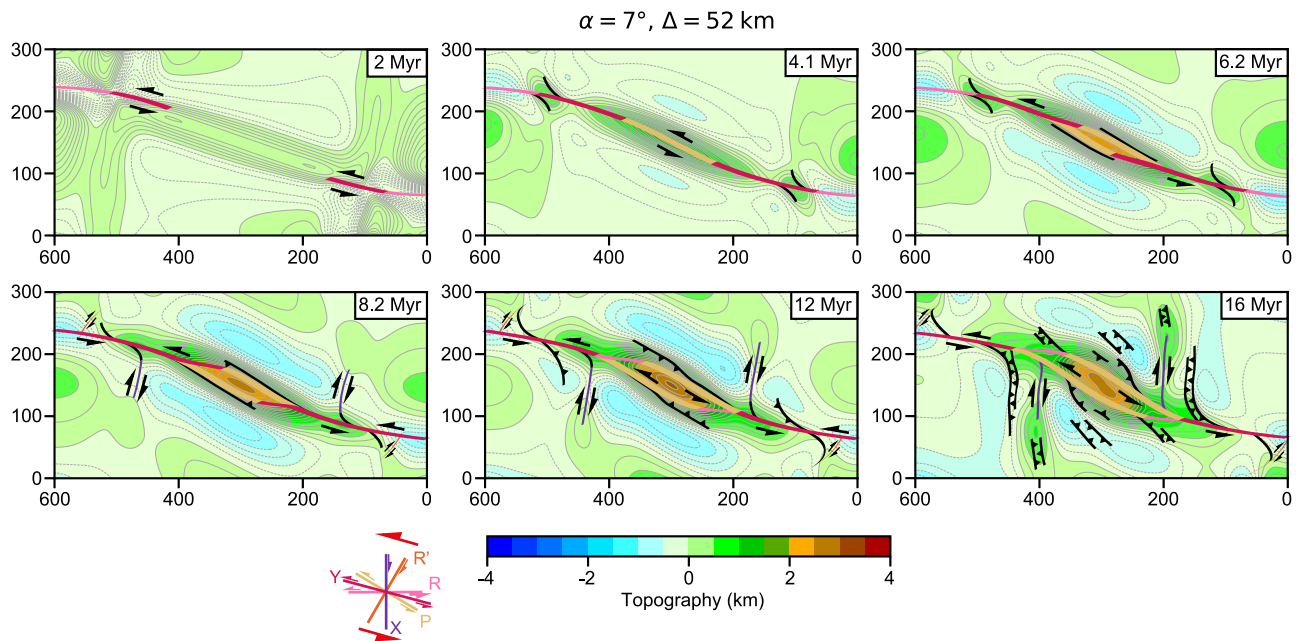


**Fig. 5 | Evolution of the model  $\alpha = 7^\circ$ ,  $\Delta = 52$  km showing the topography and the interpretation of the active deformation.** The inset shows the orientation of the different shear zones in map view<sup>6,56,57</sup>.

forming a new duplex structure. To the south, an additional P-shear emerges, running parallel to the central and western P-shears to link the two principal shear zones. These P-shear zones exhibit transtensional to extensional deformation in their central segments, while thrust faults form around them, generating pop-up structures and flexural basins. The development of these new faults leads to a redistribution of slip rates across the system, resulting in decreased activity on the principal shear zones.

Finally, at 16 Myrs, the P-shear zones gradually lose prominence as deformation shifts to thrust faults, further accentuating topography. Additionally, right-lateral shear zones develop between the parallel left-lateral shear zones to accommodate the rotation generated by their interaction. Slip rates continue to redistribute across the evolving fault system.

### Strain localization and fault interaction

Our models reveal three distinct evolutions governed by the initial geometric configuration, specifically the angle  $\alpha$  and the spacing  $\Delta$  between the two weak zones (Fig. 3). A clear distinction arises between the first group of models, which develop sigmoidal push-up structures, and the second and third groups, which form parallel strike-slip faults that may or may not interact to produce duplex systems, depending on  $\Delta$ , the distance between the initial weak zones in the direction perpendicular to the boundary velocity field.

The angle  $\alpha$  primarily controls whether deformation localizes into a single push-up structure or into multiple parallel shear zones. A critical threshold occurs at  $\alpha = 15^\circ$ , which corresponds to an angle of  $\phi/2$ , where  $\phi$  is the internal friction angle of the material. This threshold aligns with the orientation of P-shears measured clockwise from Y-shears. For angles below this threshold, shear zones remain relatively aligned and interact to form a push-up structure. At larger angles, the system favors the development of parallel shear zones, with their interaction dependent on  $\Delta$ .

While  $\Delta$  plays a limited role in the formation of push-up structures, it becomes a key parameter for duplex systems. When the spacing between the weak zones is too large, the two strike-slip faults that emerge from the weak zones do not interact, preventing the formation of a duplex system. Conversely, at smaller spacings, interaction occurs,

leading to the emergence of internal restraining bends and duplex-like architectures.

Push-up and duplex systems also differ in how they accommodate shortening and in their temporal evolution. Push-up systems typically develop as a single lithospheric-scale shear zone that distributes deformation into the crust, growing by initiating new thrusts that propagate outward from the restraining bend. In contrast, duplex systems consist of a network of lithospheric-scale, parallel strike-slip shear zones. Within these, shortening is accommodated by oblique P-shears forming restraining bends. However, because the central restraining bends are confined between the main shear zones, thrust propagation is inhibited. Instead of outward growth, these systems evolve by initiating new restraining bends, often accompanied by the development of secondary Y-shears, as deformation continues (e.g., Fig. 7, 12 Myr). Nevertheless, our models reveal a vertical gradient in strain localization, with multiple shear zones developing near the surface, whereas single larger-scale shear zones persist at depth. This behavior likely results from a greater stress drop at depth for an equivalent frictional weakening combined with shear heating that locally reduces the viscosity in the deeper parts of the crust and lithospheric mantle.

An interesting by-product of these contrasting styles of deformation at depth is that as the duplex accommodates the transpression at the crustal scale, therefore only exhumes lower crustal material within the restraining bends where erosion is high (Fig. 6 and supplementary material Figs. 10 to 18) while lithospheric scale push-up lead to the exhumation of mantle rocks (Fig. 4 and supplementary material Figs. 2 to 9).

Moreover, Figs. 4 and 6 illustrate how the fault network evolves over time, how slip rates redistribute as new faults form and interact, and how faults connect with each other in space. Fault connectivity and fault system interaction has implications for earthquake rupture dynamics and seismic hazard, particularly since fault geometries often remain difficult to constrain at depth. Fault connectivity may govern whether dynamic rupture remains confined to a single fault segment or cascades through an entire fault system [e.g., refs. 63–67]. Where unfavorably oriented gaps or rheologically strong patches decouple neighboring strands, dynamic ruptures tend to arrest, limiting event

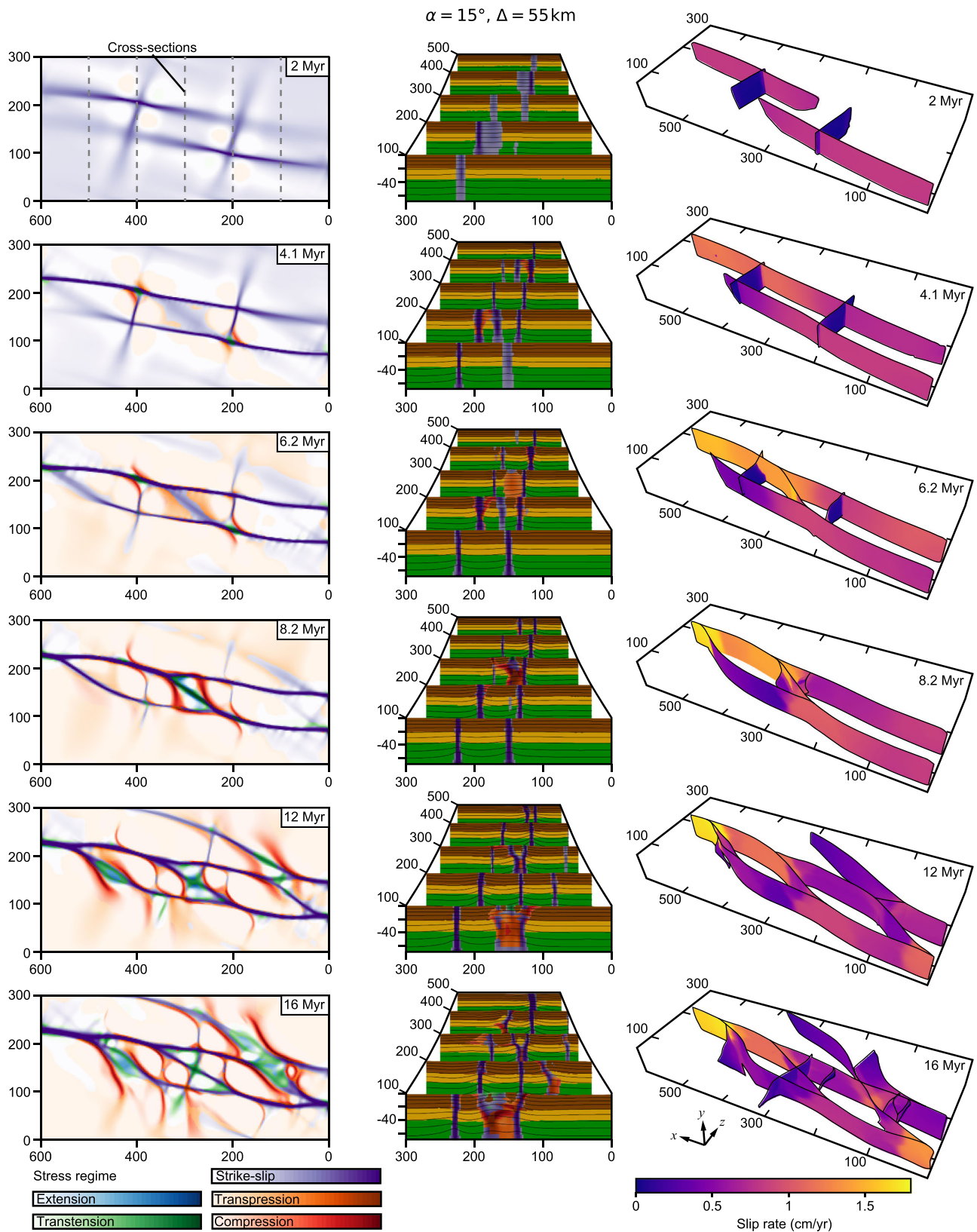


**Fig. 6 | Evolution of the model  $\alpha = 15^\circ, \Delta = 55 \text{ km}$ .** Left column shows the stress regime of the active deformation. The central column shows serial cross-sections with the stress regime superimposed. Right column shows the long-term slip-rate

on the faults. Fault surfaces are reconstructed following<sup>108</sup>. Slip-rate estimation method is detailed in “Slip-rate estimation”.

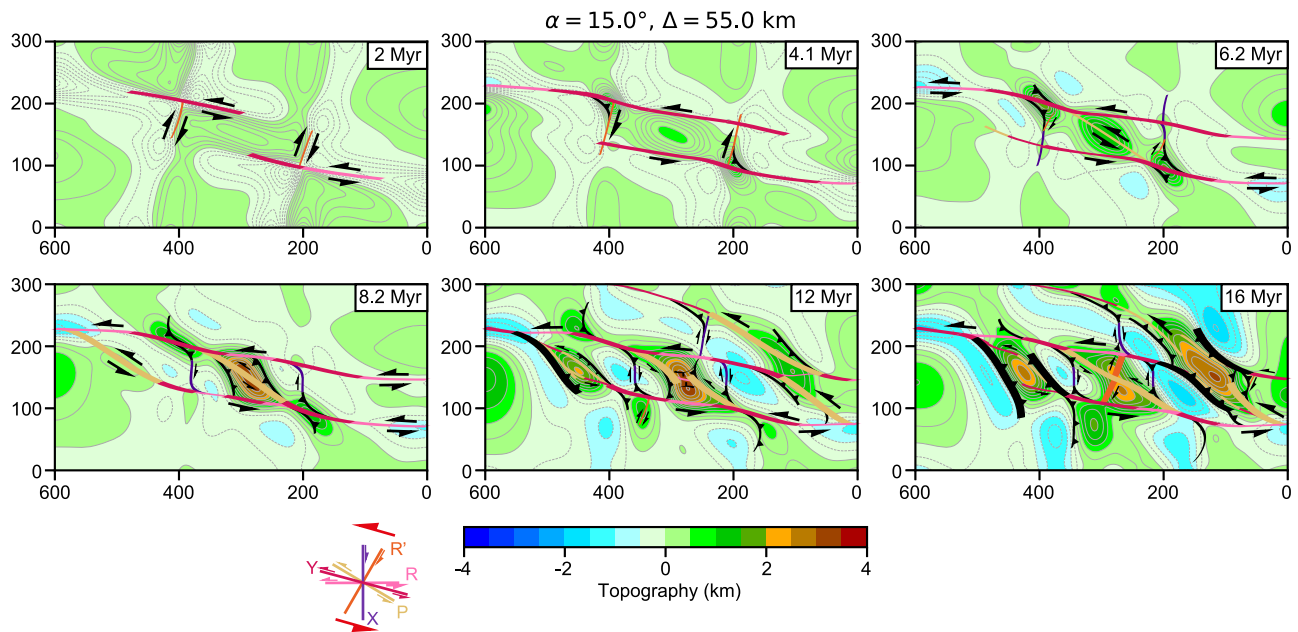


**Fig. 7 | Evolution of the model  $\alpha = 15^\circ$ ,  $\Delta = 55$  km showing the topography and the interpretation of the active deformation.** The inset shows the orientation of the different shear zones in map view<sup>6,56,57</sup>.

size [e.g., refs. 68,69]. By contrast, geometrically linked segments can foster through-going rupture and hence larger-magnitude earthquakes<sup>70</sup>, as documented for the 2019 Ridgecrest sequence and the 2016 Kaikōura cascade<sup>71–73</sup>. In this context, our long-term geodynamic models can be coupled with dynamic rupture and seismic cycle simulations [e.g., refs. 74–78] to explore the influence of fault geometry and connectivity on earthquake rupture dynamics and help interpret the connectivity of the complex natural strike-slip fault network at depth.

### Comparison with previous experiments

Numerical simulations provide a valuable complement to laboratory experiments and can help bridge the gap between surface observations and deep lithospheric processes, especially in regions where direct imaging remains limited. However, modeling strike-slip systems over geological timescales (>1 Ma) and at high finite strain (>1) poses several fundamental challenges. Numerical experiments have only recently reached the level of maturity required to complement the substantial body of knowledge derived from scaled laboratory models [e.g.,<sup>47</sup>], which are comprehensively reviewed in ref. 24.

In scaled laboratory experiments of restraining bends [e.g., refs. 20,26,27], deformation typically localizes into sigmoidal push-up structures bounded by thrusts, while P-shears are rarely observed (Fig. 8b). The predominance of thrust faults and the scarcity of P-shears in these experiments likely result from the boundary conditions used, which do not balance lateral inflow and outflow of material. This imbalance promotes vertical thickening and favors the widespread formation of thrusts to accommodate shortening. These studies consistently highlight restraining bend angle as the primary control on structural evolution, with step-over distance playing a secondary role, an observation that aligns with our own results for push-up systems, which exhibit limited sensitivity to  $\Delta$  (Fig. 3).

The principal distinction between our numerical models and previous Riedel-type experiments lies in the sequence and nature of shear zone development. Traditional Riedel-type setups impose one or several basal velocity discontinuities, which naturally favor the sequential development of R-shears above the discontinuities until they coalesce into Y-shears (Fig. 8a). This result is consistently reproduced by laboratory experiments [e.g., refs. 1,17,33–39] even in

presence of a ductile layer [e.g., ref. 36] and numerical models<sup>79</sup>. In contrast, our approach does not require pre-imposed discontinuities, leading to the direct development of Y-shears without previous R-shears. Depending on the geometric configuration, these Y-shears may evolve into P-shears (in push-up systems, Fig. 8e), develop into networks of anastomosing transpressional zones (in duplex systems, Fig. 8f), or remain subparallel (in non-interacting, parallel shear configurations, Fig. 8d). R-shears are uncommon in our models and tend to form only at the lateral edges of the domain (Figs. 5, 7 & 8). From this perspective, Riedel-type analog experiments are best suited to investigate shallow upper crust fault linkage in the presence of pre-existing discontinuities such as early en-échelon faulting, whereas our models are designed to explore how large-scale shear zones initiate and evolve in the crust and lithospheric mantle without such constraints.

Moreover, the early formation of Y-shears in our models is consistent with recent numerical simulations employing periodic boundary conditions in the shear direction, which allow for the progressive localization of deformation along the domain edges<sup>47</sup>. In contrast, numerical and analog models using pure-shear boundary conditions in map view [e.g., refs. 80,81] often find that strike-slip faults first develop in transtension, forming at the Coulomb angle to  $\sigma_1$  i.e., with the orientation of an R-shear, before rotating toward Y-shear orientations as deformation localizes and becomes increasingly transpressive.

Importantly, this distinction is not contradictory but complementary: the early formation of R-shears in analog experiments may reflect near-surface mechanics or reactivation within inherited zones [e.g., refs. 22,23,51], while the predominance of Y-shears in our simulations highlights processes that dominate at the lithospheric scale where deformation localizes progressively. Considering both perspectives thus provides a more complete framework for interpreting strike-slip systems across scales, from meter-scale outcrop observations<sup>3,4,6,82</sup> to kilometer-scale lithospheric dynamics.

### Comparison with natural systems

Natural strike-slip systems may not necessarily form above an already localized lithospheric-scale shear zone. Yet in natural systems, strain often localizes along pre-existing heterogeneities, such as thermal anomalies, lithological contacts, or inherited faults, which we represent in our models as initial weak zones. These inherited structures

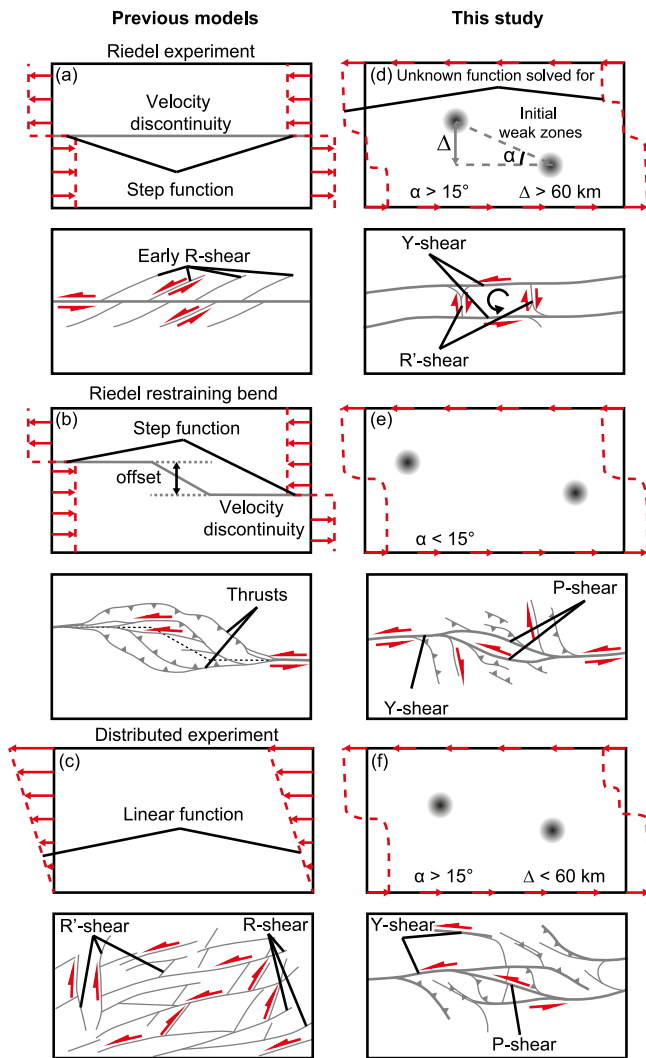


**Fig. 8 | Comparison between previous experiments and models of this study.**

Red arrows and dashed curves indicate the boundary velocity function. **a** Riedel-type experiment [e.g., ref. 117,33–39] showing early formation of R-shears coalescing into a Y-shear above the imposed velocity discontinuity. **b** Riedel-type restraining bend experiment [e.g., refs. 20,26,27] showing the formation of a sigmoidal push-up structure above an imposed velocity discontinuity. **c** Distributed shear experiment [e.g., refs. 31,32] showing the formation of parallel R-shear zones and antithetic R'-shear zones. **d** Models of this study for  $\alpha > 15^\circ$  and  $\Delta > 60$  km showing the formation of parallel Y-shear zones with limited interaction. **e** Models of this study for  $\alpha < 15^\circ$  showing the formation of a sigmoidal push-up structure where the main Y-shear zone splits into two P-shear zones around which thrusts accommodate shortening. **f** Models of this study for  $\alpha > 15^\circ$  and  $\Delta < 60$  km showing the formation of duplex structures with parallel Y-shear zones interacting by hard-linkage through P-shear zones around which thrusts accommodate shortening.

may be reactivated or partially overprinted by newly formed faults. To discuss our models results in the context of natural systems, we focus on two natural examples of restraining bends: (1) the Jamaican strike-slip fault network which illustrates strikingly the duplex architecture that we produce in our simulations and (2) the Levant Fault in Lebanon which we interpret as a large push-up structure composed of two topographic highs separated by a central depression.

**Jamaica.** Jamaica (Fig. 9) exhibits a complex fault network and deformation history shaped by evolving local stress fields and super-imposed tectonic events. It is a typical example of a restraining bend, where the Enriquillo-Plantain Garden and Walton faults (EPGF) define a

set of nearly parallel strike-slip faults that merge within the uplifted Blue Mountain Massif<sup>83–86</sup>. GNSS-based models show that the offshore sections of the EPGF accommodate approximately  $1 \text{ cm yr}^{-1}$  of left-lateral motion eastward and westward of Jamaica<sup>87</sup> while on-shore, the Jamaican fault network distributes the slip rate across faults accommodating between 3 and  $5 \text{ mm yr}^{-1}$ <sup>188</sup>. Our model (Fig. 6 at 16 Myrs) shows a similar behavior, with the southernmost fault accommodating around  $1.2 \text{ cm yr}^{-1}$  of left-lateral motion, the westernmost fault accommodating around  $1.5 \text{ cm yr}^{-1}$ , and the central fault network accommodates a distributed slip-rate between 2 and  $5 \text{ mm yr}^{-1}$ .

The northern part of Jamaica lies at the edge of the North Caribbean plate boundary<sup>13,89,90</sup> along the Cayman Basin, an ocean-floored pull-apart basin that rifted during the Paleocene-Early Eocene and has been continuously opening since<sup>91</sup>.

The Jamaican fault system marks the boundary between the thinned continental/island arc crust of the Gonâve Microplate and the Nicaragua Rise, and a thicker oceanic plateau to the southeast. The Walton Fault, and its continuation into the EPGF comprise the “inactive” branch of the Cayman pull-apart basin. With the onset of collision between the Gonâve Microplate and Hispaniola in the Early Miocene, the Walton Fault and EPGF began accommodating left-lateral motion. The lateral offset between the two faults is approximately 55 km, forming a well-defined restraining bend.

NW-SE trending folds in Jamaica are early structures (Late Cretaceous) and are sealed by Eocene-Miocene platform sediments (Yellow and White Limestone formations<sup>92</sup>). These folds are cross-cut by a long fault in a P-shear position and a penetrative network of joints and normal faults. Notably, the strike-slip fault fades and ultimately ceases within the Blue Mountain Massif, suggesting limited cumulative displacement. Its geometry and timing are consistent with P-shear formation during the early development of a duplex system, as shown in our models (Figs. 6 & 7, 6 Myrs). Normal faults reactivate the fold of the flanks of the N-S folds and induce broad, though moderate, tilting of the platform. The prominent topography (2256 m) and lower crust exhumation in the Blue Mountains, east of the duplex system, align with the late-stage, crustal-scale uplift predicted in our simulations (Fig. 7, 16 Myrs), implying that this uplift is a recent crustal-scale feature.

Our models reproduce several key features of the Jamaican restraining bend, including the formation of elongated E-W folds along the northern coast and the localization of deformation into a duplex system. The prominent topography and crustal exhumation in the Blue Mountains, east of the duplex, is consistent with late-stage, crustal-scale uplift predicted in our models (Fig. 7, 16 Myr). This suggests that uplift of the Blue Mountains is a relatively recent event. Notably, this region is also the most seismically active area in Jamaica today.

Marine geophysical surveys reveal that active offshore strike-slip faults likely extend the onshore Bull Bay Fault system, implying that transpressional strain in southeast Jamaica is accommodated across a broader network of onshore and offshore structures than previously recognized<sup>93</sup>. This offshore connectivity supports the view that restraining bends in Jamaica may localize complex fault interactions not only laterally, but also vertically and across structural domains previously considered inactive.

**Levant Fault.** The central segment of the Levant Fault in Lebanon (Fig. 10) splits into two branches forming a restraining bend that does not propagate farther north or south. Strike-slip slip-rate models along the Lebanon segment of the Levant Fault predict left-lateral slip-rates between  $2.5 \text{ mm yr}^{-1}$ <sup>194</sup> and  $5 \text{ mm yr}^{-1}$ <sup>195,96</sup>, corresponding to accommodation of 17% to 33% of the far field plate motion of  $-1.5 \text{ cm yr}^{-1}$ <sup>195,96</sup>. In our model, the strike-slip fault branches accommodate slip-rates of  $-0.6 \text{ cm yr}^{-1}$  at 16 Myrs (Fig. 4) for a far-field plate velocity of  $2 \text{ cm yr}^{-1}$ , which represents 30% of the total plate velocity. Instead, the deformation fades into a network of NE-SW trending faults and tight

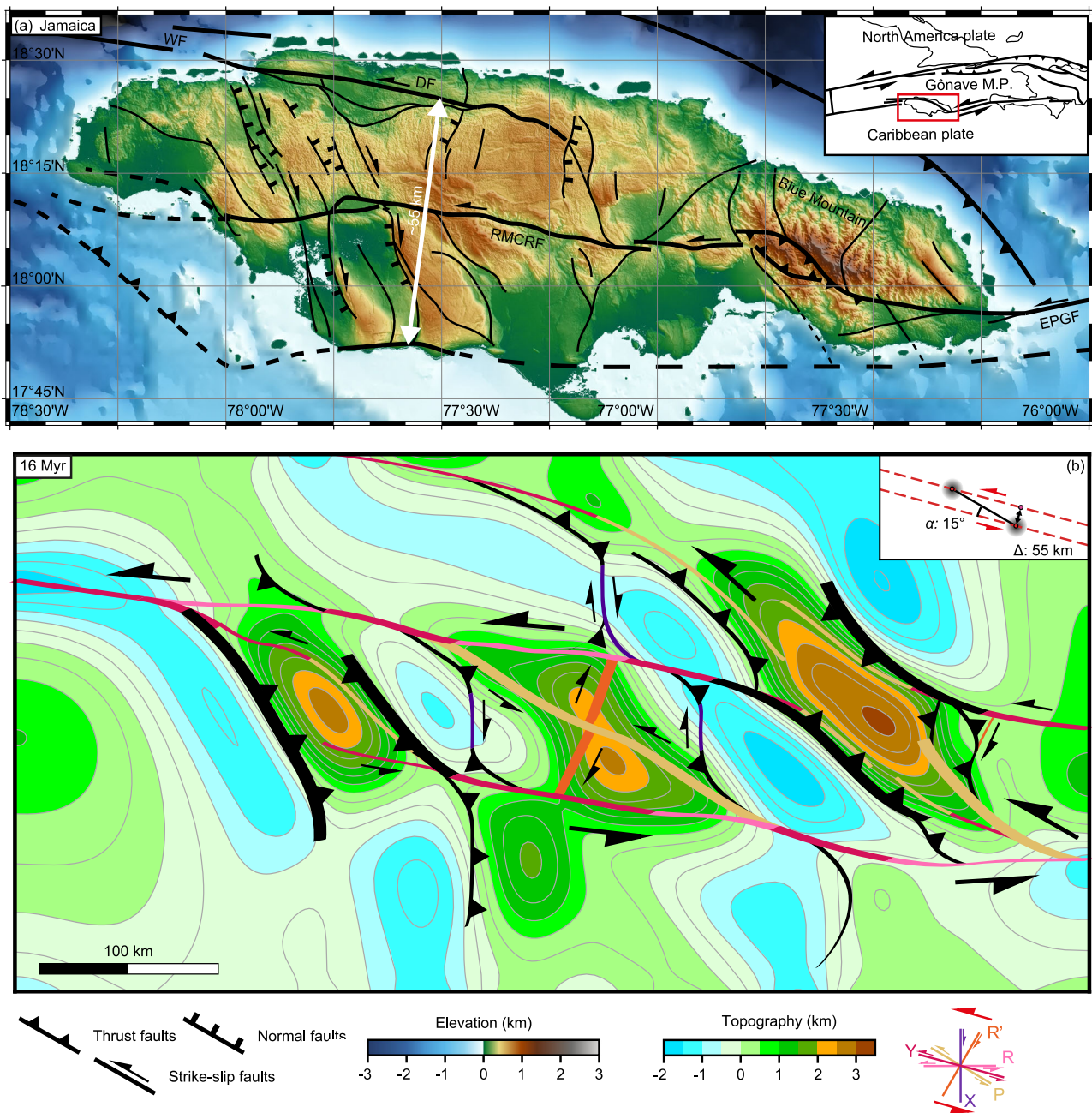


**Fig. 9 | Jamaican fault network.** **a** Topographic map of Jamaica with the principal faults from<sup>83–86,88</sup>. DF: Duanvale Fault, EPGF: Enriquillo-Plantain Garden Fault, WF: Walton Fault, RMCRF: Rio Minho-Crawle River Fault, M.P.: Micro Plate. **b** Model

$\alpha = 15^\circ$ ,  $\Delta = 55$  km at 16 Myrs showing the topography and the interpretation of the active deformation.

folds and thrusts<sup>97</sup>, similar to the thrusts forming in our push-up model at 12 and 16 Myrs (Figs. 4 & 5). These thrusts form both east of the restraining bend in the Palmyrides and westward in the offshore Levant Basin<sup>98</sup>.

The orientation of these thrusts matches the predictions from our model (Figs. 4 & 5). However, in nature, their direction is also influenced by the reactivation of inherited Early Mesozoic rift basins that were inverted during Late Cretaceous and Early Cenozoic compression. This case illustrates the development of a wide crustal-scale push-up underlain by a lithospheric left-lateral shear zone marking the boundary between the Arabian and African plates.

The topography along the Levant Fault is characterized by two prominent mountain ranges, Mount Lebanon and Anti-Lebanon,

separated by the Bekaa Valley depression, a normal fault-bounded synclinorium [e.g., refs. 15,99,100]. This topography and the associated faults correspond to the transtensional region predicted at the core of the lithospheric-scale push-up in our simulations (Fig. 4, 12 and 16 Myrs). Further investigation using seismic imaging could help test whether lower crust and mantle exhumation occur beneath the Bekaa Valley, as suggested by our model predictions.

## Discussion

Our 3D lithospheric-scale experiments allow the spontaneous development of strike-slip fault systems without imposing predefined velocity discontinuities or fault geometries. This setup enables the systematic investigation of how inherited weak zones control strain

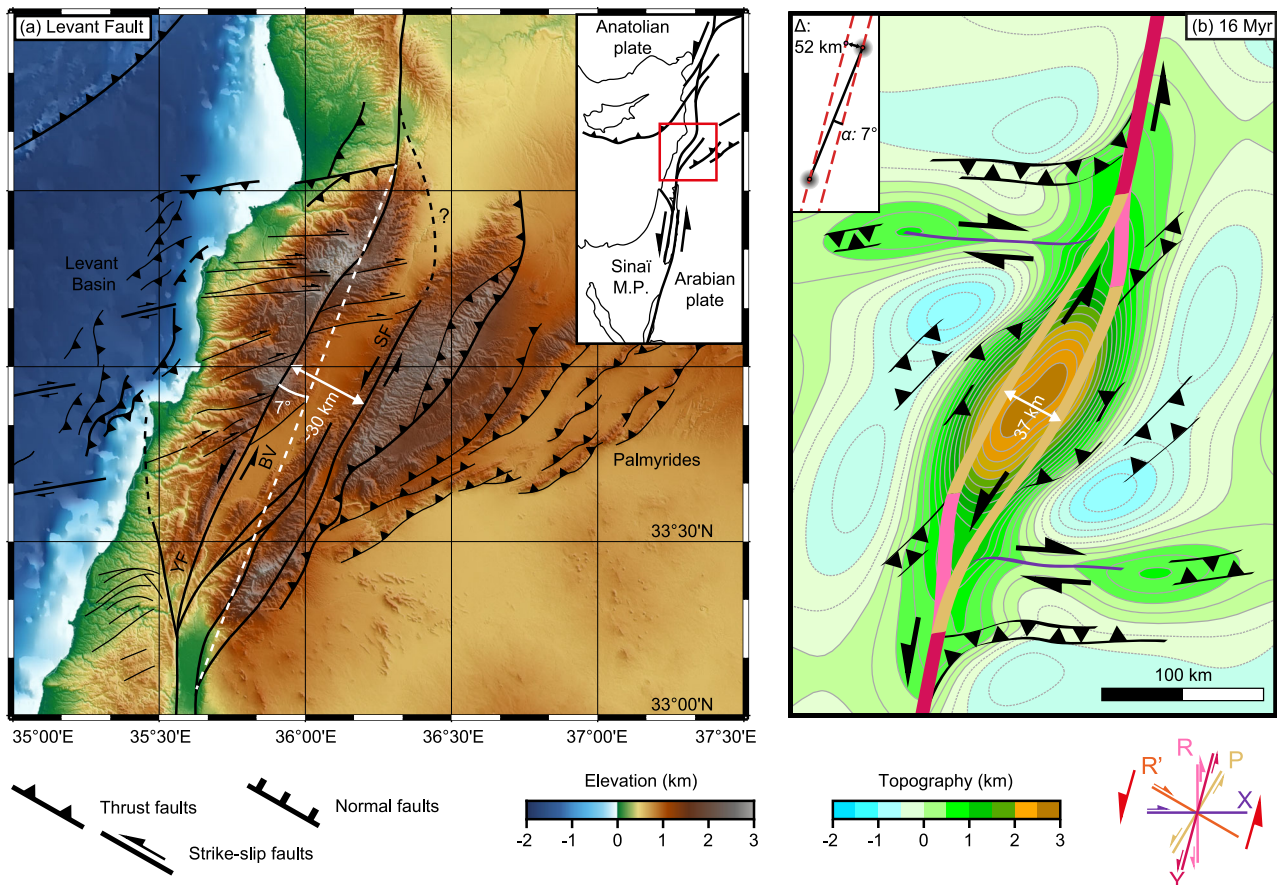


**Fig. 10 | Levant fault.** **a** Topographic map of the Levant Fault with the principal faults from<sup>15,97,98</sup>. YF: Yammouneh Fault, SF: Serghaya Fault, BV: Bekaa Valley, M.P.: Micro Plate. **b** Model  $\alpha = 7^\circ$ ,  $\Delta = 52$  km at 16 Myrs showing the topography and the interpretation of the active deformation.

localization and the formation of restraining bends in transpressional plate boundary settings.

We find that the geometry of weak zones exerts a primary control on the structural style and evolution of strike-slip systems. When the angle between inherited weak zones is smaller than half the internal friction angle ( $<15^\circ$ ), deformation localizes into a single lithospheric-scale push-up structure, largely independent of the spacing between weak zones. In contrast, for larger angles ( $\geq 15^\circ$ ), duplex systems develop only when the spacing is smaller than about 60 km (for the adopted rheology), whereas greater spacing leads to parallel, non-interacting strike-slip faults that accommodate limited deformation between them.

Push-up systems and duplex systems also display fundamentally different tectonic evolution and shortening accommodation. Push-up systems form as single, lithospheric-scale shear zones that distribute deformation into the surrounding crust and evolve by sequential initiation of thrusts propagating outward from the restraining bend. Duplex systems, in contrast, evolve as networks of parallel strike-slip shear zones that generate new restraining bends and secondary Y-shears, which accommodate additional strain. This hierarchical pattern of strain localization explains why, in Jamaica, seismicity tends to cluster along the youngest and most external structures, while more diffuse activity persists across older fault segments<sup>85,88,101,102</sup>.

When applied to natural examples, our results help interpret the structural and seismic complexity of restraining bends such as the Levant and Jamaican fault systems. In the Levant, the modeled push-up configuration reproduces the observed organization of the Levant Fault, where the Yammouneh and Serghaya branches enclose the Bekaa Valley, with thrusts propagating offshore into the Levant Basin and onshore into the Palmyrides (Fig. 10). In Jamaica, the duplex

configuration captures the interaction of parallel strike-slip faults responsible for the uplift of the Blue Mountain massif and the spatial distribution of seismicity across the island. Moreover, the capacity for deep strain localization and partial mantle exhumation in our models may explain the absence of crustal roots and the presence of high-velocity bodies in the middle crust beneath certain push-up systems, such as those observed in the western Transverse Ranges of California<sup>103</sup>.

Overall, these experiments provide a self-consistent framework for linking surface faulting with deep lithospheric processes. By combining realistic, non-linear, thermally dependent rheology with unconstrained fault development, our models bridge the gap between laboratory-scale analog experiments and natural lithospheric systems, offering a powerful tool for interpreting the long-term evolution and seismic potential of restraining bends in lithospheric-scale strike-slip systems.

## Methods

### Governing equations

The long-term deformation of the lithosphere is simulated by solving the conservation of momentum and mass for an incompressible fluid with non-linear viscosities:

$$\nabla \cdot \underline{\underline{\sigma}}(\mathbf{u}, p, T) + \rho(p, T)\mathbf{g} = \mathbf{0}, \quad (1)$$

$$\nabla \cdot \mathbf{u} = 0, \quad (2)$$

where  $\mathbf{u}$  represents velocity,  $p$  is pressure,  $T$  the temperature,  $\rho(p, T)$  is density, and  $\mathbf{g}$  is the gravitational acceleration vector. The stress

tensor,  $\underline{\sigma}$ , can be decomposed into deviatoric and isotropic components such that  $\underline{\sigma}(\mathbf{u}, p, T) := \underline{\tau}(\mathbf{u}, p, T) - p\underline{\mathbf{I}}$ , where  $\underline{\mathbf{I}}$  is the identity matrix. The deviatoric stress tensor,  $\underline{\tau}$ , is given by:

$$\underline{\tau}(\mathbf{u}, p, T) := 2\eta(\mathbf{u}, p, T)\dot{\underline{\underline{\epsilon}}}(\mathbf{u}), \tag{3}$$

with  $\eta$  as the non-linear viscosity and

$$\dot{\underline{\underline{\epsilon}}}(\mathbf{u}) := \frac{1}{2}(\nabla\mathbf{u} + \nabla\mathbf{u}^T) \tag{4}$$

as the strain-rate tensor.

For the volume forces, we adopt the Boussinesq approximation, where density is expressed as:

$$\rho(p, T) := \rho_0(1 - \alpha(T - T_0) + \beta(p - p_0)) \tag{5}$$

with  $\rho_0$  representing the reference density at  $T = T_0$  and  $p = p_0$ ,  $\alpha$  the coefficient of thermal expansion and  $\beta$  the coefficient of compressibility.

Finally, given the temperature dependence of both viscosity and density, we also solve for thermal energy conservation:

$$\rho_0 C_p \left( \frac{\partial T}{\partial t} + \mathbf{u} \cdot \nabla T \right) - \nabla \cdot (k \nabla T) = H_0 + H_s \tag{6}$$

where  $C_p$  is the specific heat capacity,  $k$  is the thermal conductivity,  $H_0$  is material-dependent heat source, such as radiogenic heat production, and  $H_s = \underline{\tau} : \dot{\underline{\underline{\epsilon}}}$  is the heat generated by mechanical work.

### Boundary conditions

To describe the boundary conditions we first define the domain boundaries  $\partial\Omega$  such that  $\partial\Omega = \Gamma_D \cup \Gamma_N \cup \Gamma_S \cup \Gamma_B$ , with

$$\begin{aligned} \Gamma_D &= \{\mathbf{x} \in \partial\Omega \mid z = O_z, z = L_z\}, \\ \Gamma_N &= \{\mathbf{x} \in \partial\Omega \mid x = O_x, x = L_x\}, \\ \Gamma_S &= \{\mathbf{x} \in \partial\Omega \mid y = L_y\}, \\ \Gamma_B &= \{\mathbf{x} \in \partial\Omega \mid y = O_y\}, \end{aligned}$$

where  $\Gamma_D$  are the boundaries on which we apply Dirichlet conditions,  $\Gamma_N$  are the boundaries on which we apply the Navier-slip conditions,  $\Gamma_S$  is the boundary on which we apply a free surface condition and  $\Gamma_B$  is the bottom boundary.

Strike-slip deformation is imposed via an heterogeneous simple shear velocity field varying non-linearly, using a recently developed Navier-slip boundary condition<sup>55</sup>. This method generalizes the classical free-slip formulation by allowing specification of an arbitrary velocity direction along the boundaries, while leaving the magnitude unconstrained. This method allows simulating strike-slip motion across the model boundaries while avoiding explicit constraints on the velocity variation across evolving shear zones. Consequently, the model exhibits more realistic behavior, allowing strain localization in the lithosphere without imposing predefined orientations or structures such as faults or discontinuities.

For detailed methodology, see refs. 55. A crucial aspect of this approach is that the constrained velocity direction cannot be perpendicular to the boundary, as null dot products would invalidate the boundary condition formulation. To satisfy this requirement, the shear direction, represented by the red dashed line in Fig. 2a, is rotated by 15° relative to the  $x$ -axis of the modeling domain. Navier-slip conditions are applied on the  $x$ -normal faces (boundaries  $\Gamma_N$ ), such that the velocity is aligned with the shear direction, while the code solves for its magnitude

resulting into either distributed (left in Fig. 2a) or localized shear (right in Fig. 2a) on the boundary. This rotation offers two major advantages:

- Rotating the shear direction is mathematically equivalent to rotating the reference frame. Since the reference frame is Galilean, the physics remain unchanged, preserving the simple shear velocity field.
- A regular and undeformed computational grid is easier to handle.

To impose the boundary conditions, we first define an analytical linear velocity function for horizontal simple shear in the  $x$  direction (Fig. 2a):

$$\bar{\mathbf{u}} \rightarrow (x, y, z) := \begin{bmatrix} \bar{u}_{L_z} - \bar{u}_{O_z} (z - 1) + \bar{u}_{L_z} \\ 0 \\ 0 \end{bmatrix} \tag{7}$$

where  $\bar{u}_{L_z}$  and  $\bar{u}_{O_z}$  are the velocities at  $z = L_z$  (1 cm yr<sup>-1</sup>) and  $z = O_z$  (-1 cm yr<sup>-1</sup>), respectively, yielding a total velocity difference of 2 cm yr<sup>-1</sup>. To apply the rotated simple shear, we transform the velocity field (Fig. 2a) defined by Eq. (7) using:

$$\bar{\mathbf{u}}_R(\mathbf{x}) = \underline{\underline{\mathbf{R}}}(\theta)\bar{\mathbf{u}}\underline{\underline{\mathbf{R}}}^T(\theta)\mathbf{x}, \tag{8}$$

where  $\mathbf{x} = [x, y, z]^T$  is the coordinates vector,  $\theta$  is the rotation angle (15°), and  $\underline{\underline{\mathbf{R}}}(\theta)$  is the rotation matrix:

$$\underline{\underline{\mathbf{R}}}(\theta) := \begin{bmatrix} \cos \theta & 0 & \sin \theta \\ 0 & 1 & 0 \\ -\sin \theta & 0 & \cos \theta \end{bmatrix},$$

which describes rotation around the vertical axis.

On the  $z$ -normal faces (the front and back of the domain, boundaries  $\Gamma_D$ ), we prescribe constant uniform simple shear velocity field using Dirichlet conditions (green arrows in Fig. 2c) described by:

$$\begin{cases} u_x = \bar{u}_{R_x}(\mathbf{x}) \\ u_z = \bar{u}_{R_z}(\mathbf{x}) \end{cases}$$

to ensure that the velocity field remains approximately divergence-free in map view when integrated over the entire domain.

Additionally, at the boundaries  $\Gamma_N$ , we maintain velocity alignment with the shear direction, enforcing  $\mathbf{u} \cdot \hat{\mathbf{n}} = 0$ , where  $\hat{\mathbf{n}}$  is the unit vector normal to the shear direction.

The Navier-slip conditions also require stress constraints. To compute these, we evaluate the strain-rate tensor of the rotated velocity field  $\dot{\underline{\underline{\epsilon}}}(\bar{\mathbf{u}}_R)$  and, at each non-linear iteration, compute the deviatoric stress  $2\eta(\mathbf{u}^k, p^k, T)\dot{\underline{\underline{\epsilon}}}(\bar{\mathbf{u}}_R)$  where  $\eta$  is the viscosity defined at Eq. (12) and evaluated using  $\mathbf{u}^k$  and  $p^k$ , the velocity and pressure obtained at the  $k^{\text{th}}$  non-linear iteration respectively.

On the top boundary  $\Gamma_S$ , we impose a free surface condition,  $\underline{\underline{\sigma}}\mathbf{n} = \mathbf{0}$ , allowing for topography development, including uplift and basin formation. At the bottom boundary ( $\Gamma_B$ ), material is allowed to flow in or out with a vertical velocity  $u_y^{\text{bot}}$  that is dynamically adjusted to compensate for mass gain or loss through the lateral boundaries. Due to the overall divergence free model boundary setup,  $u_y^{\text{bot}}$  remains close to zero throughout the simulation.

To solve the thermal energy conservation (Eq. (6)) we impose the following boundary conditions:

$$\begin{aligned} T = 0^\circ\text{C} & \quad \forall \mathbf{x} \in \Gamma_S \\ T = 1450^\circ\text{C} & \quad \forall \mathbf{x} \in \Gamma_B \\ k\nabla T \cdot \mathbf{n} = 0 & \quad \forall \mathbf{x} \in \Gamma_D \cup \Gamma_N. \end{aligned}$$

### Rheological model

To simulate the long-term deformation of both the lithosphere and asthenosphere, we adopt a visco-plastic formulation. The brittle regions of the lithosphere are described by the Drucker-Prager yield criterion:

$$\sigma_y(p) := C \cos \phi + p \sin \phi$$

where  $C$  is the material cohesion and  $\phi$  the friction angle.

The viscosity associated with plastic deformation is computed as:

$$\eta_p(\mathbf{u}, p) := \frac{\sigma_y(p)}{\dot{\underline{\underline{\varepsilon}}}}(\mathbf{u}), \quad (9)$$

where

$$\dot{\underline{\underline{\varepsilon}}}(\mathbf{u}) := \sqrt{\frac{1}{2} \dot{\underline{\underline{\varepsilon}}}(\mathbf{u}) : \dot{\underline{\underline{\varepsilon}}}(\mathbf{u})}$$

represents the second invariant of the strain-rate tensor. To capture fault weakening processes, we incorporate plastic strain-dependent softening. We first compute the plastic strain at a given time  $t_1$  as:

$$\varepsilon_p(t_1) = \varepsilon_p(t_0) + \int_{t_0}^{t_1} \dot{\varepsilon}_p dt,$$

where

$$\dot{\varepsilon}_p = \begin{cases} \dot{\underline{\underline{\varepsilon}}}(\mathbf{u}) & \text{if } \eta_p < \eta_v \\ 0 & \text{otherwise} \end{cases}$$

subject to the initial condition  $\varepsilon_p(t = 0)$  described by Eq. (13). Then, we define the function describing the softening of plastic parameters as:

$$\chi(\varepsilon_p, \chi_0, \chi_1) := \begin{cases} \chi_0 & \text{if } \varepsilon_p \leq \varepsilon_0 \\ \chi_0 - \frac{\varepsilon_p - \varepsilon_0}{\varepsilon_1 - \varepsilon_0} (\chi_0 - \chi_1) & \text{if } \varepsilon_0 < \varepsilon_p < \varepsilon_1, \\ \chi_1 & \text{otherwise} \end{cases} \quad (10)$$

where  $\chi_0$  and  $\chi_1$  are respectively the initial and fully softened values of  $\chi$ , the parameter to be softened, and  $\varepsilon_p$  is the accumulated plastic strain. The parameters  $\varepsilon_0$  and  $\varepsilon_1$  define the onset and completion of softening. Therefore, the friction angle and the cohesion evolve with accumulated plastic strain such that  $\phi := \phi(\varepsilon_p, \phi_0, \phi_1)$  and  $C := C(\varepsilon_p, C_0, C_1)$ .

For the viscous regions of the lithosphere and asthenosphere, we use a dislocation creep law governed by the Arrhenius equation:

$$\eta_v(\mathbf{u}, p, T) := A^{-1} \dot{\underline{\underline{\varepsilon}}}(\mathbf{u})^{\frac{1}{n}-1} \exp\left(\frac{Q+pV}{nRT}\right) \quad (11)$$

where  $A$  is the pre-exponent factor,  $n$  the stress exponent,  $Q$  the activation energy,  $V$  the activation volume for a given material and  $R$  is the gas constant.

Finally, the effective viscosity of the material is computed as the minimum of the plastic and viscous viscosities:

$$\eta(\mathbf{u}, p, T) := \min(\eta_p, \eta_v). \quad (12)$$

### Initial geometry

We define the modeled domain as a rectangular cuboid in  $\mathbb{R}^3$ , given by  $\Omega = [O_x, L_x] \times [O_y, L_y] \times [O_z, L_z]$ , where  $O_x = 0$ ,  $O_y = -250$  km,  $O_z = 0$  and

$L_x = 600$  km,  $L_y = 0$ ,  $L_z = 300$  km. Here, the  $x$  and  $z$  directions form the horizontal plane, while  $y$  corresponds to the vertical direction.

We discretize the domain using  $256 \times 64 \times 128 Q_2 - P_1^d$  elements for velocity and pressure. The mesh is uniform in the horizontal ( $x$  and  $z$ ) directions, while vertical ( $y$ ) direction mesh refinement is applied to enhance resolution in the crust and lithospheric mantle relative to the asthenosphere. Specifically, the vertical mesh is refined as follows:

- 22 elements between 0 and -16 km,
- 24 elements between -16 km and -50 km,
- 18 elements between -50 km and -250 km.

This stratified refinement ensures greater detail in the lithosphere, where deformation is most significant.

We define the initial model geometry with four stratified and initially flat layers, each corresponding to a specific lithospheric or asthenospheric material. The vertical extents and rheological representations of these layers are as follows:

- the upper crust, extending from  $y=0$  to  $y=-20$  km, is modeled using a quartz rheology<sup>104</sup>,
- the lower crust, extending from  $y=-20$  km to  $y=-35$  km, is modeled using an anorthite rheology<sup>105</sup>,
- the lithospheric mantle, extending from  $y=-35$  km to  $y=-115$  km, is modeled using an olivine rheology<sup>106</sup>,
- the asthenosphere, extending from  $y=-115$  km to  $y=-250$  km, is also modeled using an olivine rheology<sup>106</sup>.

All rheological parameters for each lithology are provided in the Supplementary Table 1.

### Initial temperature

The initial temperature field is computed by solving the steady-state heat equation:

$$-\nabla \cdot k \nabla T = H_0.$$

To ensure the 1300°C isotherm lies at  $y=-105$  km, the thermal conductivity in the asthenosphere is set to  $k = 70 \text{ W.m}^{-1}.\text{K}^{-1}$ .

### Initial weak zones

In this study, we aim to explore how and when strike-slip faults interact and link to form restraining bends. To do so, we must control and vary both the distance between the faults and the initial obliquity of their interactions without prescribing the fault orientation. To achieve this, we use the sum of two Gaussian functions to prescribe the initial plastic strain scalar field<sup>78</sup>:

$$\begin{aligned} \varepsilon_p(\mathbf{x}, t=0) &:= \text{rand}(\varepsilon_0, \varepsilon_1) \sum_{i=1}^2 \left( \prod_{d=1}^3 \exp(-a(x_d - C_{di})^2) \right) \\ &= \text{rand}(\varepsilon_0, \varepsilon_1) \sum_{i=1}^2 \left( e^{-a(x_0 - C_{0i})^2} \cdot e^{-a(x_1 - C_{1i})^2} \cdot e^{-a(x_2 - C_{2i})^2} \right) \\ &= \text{rand}(\varepsilon_0, \varepsilon_1) \sum_{i=1}^2 \left( e^{-a((x_0 - C_{0i})^2 + (x_1 - C_{1i})^2 + (x_2 - C_{2i})^2)} \right), \end{aligned} \quad (13)$$

where  $a = 1.8 \times 10^{-9}$  controls the width of the Gaussians, and

$$\underline{\underline{\mathbf{C}}} := [\mathbf{c}_1, \mathbf{c}_2] = \begin{bmatrix} C_{01} & C_{02} \\ C_{11} & C_{12} \\ C_{21} & C_{22} \end{bmatrix} \in \mathbb{R}^{3 \times 2},$$

is the matrix containing the coordinates of the centers of the two Gaussians. Using the same parameter  $a$  for all three dimensions ensures that the weak zones are spherical.

This results in two initial weak zones, as the plastic strain distribution reduces both friction angle and cohesion according to Eq. (10). These zones impose geometrical constraints, namely: the initial location of the faults, and the distance  $\Delta$  between them, in the direction normal to the simple shear imposed by the boundary conditions. The weak zones also allow us controlling the obliquity of the eventual fault linkage via the angle  $\alpha$ , formed between the direction of the imposed Gaussians and the direction of simple shear applied at the model boundaries. Note that in the classical statistical definition of a Gaussian distribution,

$$\alpha = \frac{1}{2\sigma^2},$$

where  $\sigma$  is the standard deviation.

All material-dependent parameters are provided in the supplementary material. Figure 2 shows a vertical cross-section together with the initial geotherm described in 4.5 and the initial yield strength envelope that results from the choice of parameters that will remain the same across all the simulations presented here.

### Surface processes

To simulate erosion-sedimentation processes at first order on the free surface we use a diffusion equation<sup>107</sup>:

$$\frac{\partial h}{\partial t} = -\nabla \cdot (\kappa \nabla h), \quad (14)$$

where  $h$  is the elevation of the surface and  $\kappa = 10^{-6} \text{ m}^2 \text{ s}^{-1}$  is the diffusivity. Note that only the coordinates of the free surface are updated and that we do not differentiate eroded and deposited material.

### Slip-rate estimation

Figures 4 and 6 show slip-rates along the modeled active faults. To estimate these slip-rates, we first reconstruct the fault surfaces from the 3D strain-rate field using the method described in ref. 108. Then, we compute the slip-rate using the velocity field variation across the fault plane. To do so we interpolate the velocity field such that  $\mathbf{u}^\pm := \mathbf{u}(\mathbf{x}_0 \pm d_f \mathbf{n})$ , where  $\mathbf{n}$  is the normal unit vector to the fault surface,  $d_f = 2 \text{ km}$  is a distance from the fault plane,  $\mathbf{x}_0$  is the initial position of the fault surface and  $\mathbf{u}^+$  and  $\mathbf{u}^-$  are the velocities on each side of the fault plane. Finally, we compute the slip-rate as  $\mathbf{u}_s := (\mathbf{u}^+ - \mathbf{u}^-)$ .

### Data availability

The data (numerical models) generated in this study have been deposited in the Zenodo repository under accession code <https://doi.org/10.5281/zenodo.17724420><sup>109</sup>. The supplementary information includes additional details on models evolution including all the duplex and push-up models presented in Fig. 3. We also provide the models results and the input file to reproduce them<sup>109</sup>.

### Code availability

The code used in this study to produce the numerical models is freely and publicly available at <https://github.com/laetitia/p/ptatin-gene> and provided in the repository containing the models results <https://doi.org/10.5281/zenodo.17724420><sup>109</sup>. The procedure and code to reconstruct the faults from the numerical models is available at <https://github.com/anthony-jourdon/GeoTEQpy> (live version) and<sup>110</sup> (version used in this article).

### References

- Tchalenko, J. S. Similarities between shear zones of different magnitudes. *Bull. Geol. Soc. Am.* **81**, 1625–1640 (1970).
- Swanson, M. T. Geometry and kinematics of adhesive wear in brittle strike-slip fault zones. *J. Struct. Geol.* **27**, 871–887 (2005).
- Swanson, M. T. Late Paleozoic strike-slip faults and related vein arrays of Cape Elizabeth, Maine. *J. Struct. Geol.* **28**, 456–473 (2006).
- Mann, P. *Global catalogue, classification and tectonic origins of restraining- and releasing bends on active and ancient strike-slip fault systems*, Vol. 290, 13–142 (Geological Society Special Publication, 2007).
- Aydin, A. & Nur, A. Evolution of pull-apart basins and their scale independence. *Tectonics* **1**, 91–105 (1982).
- Christie-Blick, N. & Biddle, K. T. Deformation and basin formation along strike-slip faults. *Soc. Econ. Paleontol. Mineral.* **37**, 1–34 (1985).
- Harding, T. P., Vierbuchen, R. C. & Christie-Blick, N. Structural styles, plate tectonic settings, and hydrocarbon traps of divergent (transtensional) wrench faults. *Soc. Econ. Paleontol. Mineral.* **37**, 51–77 (1985).
- Aydin, A. & Nur, A. The types and role of stepovers in strike-slip tectonics. *Soc. Econ. Paleontol. Mineral.* **37**, 35–44 (1985).
- Woodcock, N. H. & Fischer, M. Strike-slip duplexes. *J. Struct. Geol.* **8**, 725–735 (1986).
- Huang, L. & Liu, C. -y Three types of flower structures in a divergent-wrench fault zone. *J. Geophys. Res.: Solid Earth* **122**, 10478–10497 (2017).
- Mengjia, Z. et al. An overview of structures associated with bends of strike-slip faults: Focus on analogue and numerical models. *Mar. Petrol. Geol.* **167**, 106983 (2024).
- Wesnousky, S. G. The San Andreas and Walker Lane fault systems, western North America: Transpression, transtension, cumulative slip and the structural evolution of a major transform plate boundary. *J. Struct. Geol.* **27**, 1505–1512 (2005).
- Calais, E. & Mercier de Lépinay, B. From transtension to transpression along the northern Caribbean plate boundary off Cuba: Implications for the recent motion of the Caribbean plate. *Tectonophysics* **186**, 329–350 (1991).
- Dalaison, M., Jolivet, R. & Le Pourhiet, L. A snapshot of the long-term evolution of a distributed tectonic plate boundary. *Sci. Adv.* **9**, eadd7235 (2023).
- Homberg, C. et al. Tectonic evolution of the central Levant domain (Lebanon) since Mesozoic time. *Geol. Soc. Spec. Publ.* **341**, 245–268 (2010).
- Dow, D. & Sukamto, R. Western Irian Jaya: the end-product of oblique plate convergence in the late Tertiary. *Tectonophysics* **106**, 109–139 (1984).
- Richard, P. D., Naylor, M. A. & Koopman, A. Experimental models of strike-slip tectonics. *Pet. Geosci.* **1**, 71–80 (1995).
- Schreurs, G. & Colletta, B. Analogue modelling of faulting in zones of continental transpression and transtension. *Geol. Soc. Lond. Spec. Publ.* **135**, 59–79 (1998).
- Dooley, T. P., McClay, K. & Bonora, M. *4D evolution of segmented strike-slip fault systems: applications to NW Europe*, Ch. Petroleum Geology of Northwest Europe: Proceedings of the 5th Conference, 215–225 (Geological Society, London, 1999).
- McClay, K. & Bonora, M. Analog models of restraining stepovers in strike-slip fault systems. *AAPG Bull.* **85**, 233–260 (2001).
- Li, Q., Liu, M. & Zhang, H. A 3-D viscoelastoplastic model for simulating long-term slip on non-planar faults. *Geophys. J. Int.* **176**, 293–306 (2009).
- Leever, K. A., Gabrielsen, R. H., Sokoutis, D. & Willingshofer, E. The effect of convergence angle on the kinematic evolution of strain partitioning in transpressional brittle wedges: Insight from analog modeling and high-resolution digital image analysis. *Tectonics* **30**, TC2013 (2011).
- Leever, K. A., Gabrielsen, R. H., Faleide, J. I. & Braathen, A. A transpressional origin for the West Spitsbergen fold-and-thrust belt: Insight from analog modeling. *Tectonics* **30**, TC2014 (2011).

24. Dooley, T. P. & Schreurs, G. Analogue modelling of intraplate strike-slip tectonics: A review and new experimental results. *Tectonophysics* **574–575**, 1–71 (2012).
25. González, D., Pinto, L., Peña, M. & Arriagada, C. 3D deformation in strike-slip systems: Analogue modelling and numerical restoration. *Andean Geol.* **39**, 295–316 (2012).
26. Cooke, M. L., Schottenfeld, M. T. & Buchanan, S. W. Evolution of fault efficiency at restraining bends within wet kaolin analog experiments. *J. Struct. Geol.* **51**, 180–192 (2013).
27. Hatem, A. E., Cooke, M. L. & Madden, E. H. Evolving efficiency of restraining bends within wet kaolin analog experiments. *J. Geophys. Res.: Solid Earth* **120**, 1975–1992 (2015).
28. Ritter, M. C., Rosenau, M. & Oncken, O. Growing faults in the lab: Insights into the scale dependence of the fault zone evolution process. *Tectonics* **37**, 140–153 (2018).
29. Liu, J. et al. Fault networks in triaxial tectonic settings: Analog modeling of distributed continental extension with lateral shortening. *Tectonics* **43**, e2023TC008127 (2024).
30. Vendeville, B., Corti, G., Boussarsar, M. & Ferrer, O. An alternative experimental configuration to generate a wrench zone above a viscous layer. *J. Struct. Geol.* **184**, 105166 (2024).
31. Gapais, D., Fiquet, G. & Cobbold, P. Slip system domains, 3. New insights in fault kinematics from plane-strain sandbox experiments. *Tectonophysics* **188**, 143–157 (1991).
32. Schreurs, G. *Fault development and interaction in distributed strike-slip shear zones: an experimental approach*, Vol. 210, 35–52 (Geological Society, London, Special Publications, 2003).
33. Naylor, M. A., Mandl, G. & Sijpesteijn, C. H. K. Fault geometries in basement-induced wrench faulting under different initial stress states. *J. Struct. Geol.* **8**, 737–752 (1986).
34. Schellart, W. P. & Nieuwland, D. A. 3D evolution of a pop-up structure above a double basement strike-slip fault: some insights from analogue modelling. *Geol. Soc., Lond. Spec. Publ.* **212**, 169–179 (2003).
35. Hatem, A. E., Cooke, M. L. & Toeneboehn, K. Strain localization and evolving kinematic efficiency of initiating strike-slip faults within wet kaolin experiments. *J. Struct. Geol.* **101**, 96–108 (2017).
36. Zusa, A. V., Yin, A., Lin, J. & Sun, M. Spacing and strength of active continental strike-slip faults. *Earth Planet. Sci. Lett.* **457**, 49–62 (2017).
37. Lefevre, M., Souloumiac, P., Cubas, N. & Klinger, Y. Experimental evidence for crustal control over seismic fault segmentation. *Geology* **48**, 844–848 (2020).
38. Jiao, L., Klinger, Y. & Scholtès, L. Fault segmentation pattern controlled by thickness of brittle crust. *Geophys. Res. Lett.* **48**, e2021GL093390 (2021).
39. Visage, S. et al. Evolution of the off-fault deformation of strike-slip faults in a sand-box experiment. *Tectonophysics* **847**, 229704 (2023).
40. Gabriel, A. M., Elston, H. M., Cooke, M. L. & Ramos Sánchez, C. F. Impact of material strength on releasing bend evolution. *Tektonika* **3**, 64–81 (2025).
41. Peltzer, G. & Tapponnier, P. Formation and evolution of strike-slip faults, rifts, and basins during the India-Asia collision: An experimental approach. *J. Geophys. Res.: Solid Earth* **93**, 15085–15117 (1988).
42. Fournier, M., Jolivet, L., Davy, P. & Thomas, J.-C. Backarc extension and collision: an experimental approach to the tectonics of Asia. *Geophys. J. Int.* **157**, 871–889 (2004).
43. Le Pourhiet, L., Huet, B., May, D. A., Labrousse, L. & Jolivet, L. Kinematic interpretation of the 3D shapes of metamorphic core complexes. *Geochem. Geophys. Geosyst.* **13**, Q09002 (2012).
44. Lechmann, S., Schmalholz, S., Hetényi, G., May, D. & Kaus, B. Quantifying the impact of mechanical layering and underthrusting on the dynamics of the modern India-Asia collisional system with 3-D numerical models. *J. Geophys. Res.: Solid Earth* **119**, 616–644 (2014).
45. Pusok, A. & Kaus, B. J. Development of topography in 3-D continental-collision models. *Geochem. Geophys. Geosyst.* **16**, 1378–1400 (2015).
46. Meyer, S. E., Kaus, B. J. & Passchier, C. Development of branching brittle and ductile shear zones: A numerical study. *Geochem. Geophys. Geosyst.* **18**, 2054–2075 (2017).
47. Heckenbach, E. et al. 3D interaction of tectonics and surface processes explains fault network evolution of the Dead Sea Fault. *Tektonika* **2**, 33–51 (2024).
48. Cocco, M. & Rice, J. R. Pore pressure and poroelasticity effects in coulomb stress analysis of earthquake interactions. *J. Geophys. Res.* **107**, ESE 2-1–ESE 2-17 (2002).
49. Bürgmann, R. & Dresen, G. Rheology of the lower crust and upper mantle: Evidence from rock mechanics, geodesy, and field observations. *Annu. Rev. Earth Planet. Sci.* **36**, 531–567 (2008).
50. Montési, L. G. J. Fabric development as the key for forming ductile shear zones and enabling plate tectonics. *J. Struct. Geol.* **50**, 254–266 (2013).
51. Gabrielsen, R. H. et al. Analogue experiments on releasing and restraining bends and their application to the study of the Barents shear margin. *Solid Earth* **14**, 961–983 (2023).
52. Ross, Z. E. et al. Hierarchical interlocked orthogonal faulting in the 2019 Ridgecrest earthquake sequence. *Science* **366**, 346–351 (2019).
53. Thatcher, W. & Hill, D. P. Fault orientations in extensional and conjugate strike-slip environments and their implications. *Geology* **19**, 1116–1120 (1991).
54. Liang, C., Ampuero, J.-P. & Pino Muñoz, D. Deep Ductile Shear Zone Facilitates Near-Orthogonal Strike-Slip Faulting in a Thin Brittle Lithosphere. *Geophys. Res. Lett.* **48**, e2020GL090744 (2021).
55. Jourdon, A., May, D. A. & Gabriel, A.-A. Generalisation of the Navier-slip boundary condition to arbitrary directions: Application to 3D oblique geodynamic simulations. <https://arxiv.org/abs/2407.12361> (2024).
56. Bartlett, W. L., Friedman, M. & Logan, J. M. Experimental folding and faulting of rocks under confining pressure. Part IX. Wrench faults in limestone layers. *Tectonophysics* **79**, 255–277 (1981).
57. Dresen, G. Stress distribution and the orientation of Riedel shears. *Tectonophysics* **188**, 239–247 (1991).
58. Le Pourhiet, L., May, D. A., Huille, L., Watremez, L. & Leroy, S. A genetic link between transform and hyper-extended margins. *Earth Planet. Sci. Lett.* **465**, 184–192 (2017).
59. Le Pourhiet, L. et al. Continental break-up of the South China Sea stalled by far-field compression. *Nat. Geosci.* **11**, 605–609 (2018).
60. Jourdon, A., Kergaravat, C., Duclaux, G. & Huguen, C. Looking beyond kinematics: 3D thermo-mechanical modelling reveals the dynamics of transform margins. *Solid Earth* **12**, 1211–1232 (2021).
61. Duclaux, G., Huismans, R. S. & May, D. A. Rotation, narrowing, and preferential reactivation of brittle structures during oblique rifting. *Earth Planet. Sci. Lett.* **531**, 115952 (2020).
62. Naliboff, J. B., Glerum, A., Brune, S., Péron-Pindivic, G. & Wrona, T. Development of 3-D rift heterogeneity through fault network evolution. *Geophys. Res. Lett.* **47**, e2019GL086611 (2020).
63. Sibson, R. H. Stopping of earthquake ruptures at dilational fault jogs. *Nature* **316**, 248–251 (1985).
64. Harris, R. A. & Day, S. M. Dynamics of fault interaction: Parallel strike-slip faults. *J. Geophys. Res.* **98**, 4461–4472 (1993).
65. Oglesby, D. D. The dynamics of strike-slip step-overs with linking dip-slip faults. *Bull. Seismol. Soc. Am.* **95**, 1604–1622 (2005).
66. Oglesby, D. Rupture termination and jump on parallel offset faults. *Bull. Seismol. Soc. Am.* **98**, 440–447 (2008).

67. Lozos, J. C. Dynamic rupture modeling of coseismic interactions on orthogonal strike-slip faults. *Geophys. Res. Lett.* **49**, e2021GL097585 (2022).
68. Wesnousky, S. G. Predicting the endpoints of earthquake ruptures. *Nature* **444**, 358–360 (2006).
69. Kase, Y. & Kuge, K. Rupture propagation beyond fault discontinuities: Significance of fault strike and location. *Geophys. J. Int.* **147**, 330–342 (2001).
70. Palgunadi, K. H., Gabriel, A.-A., Garagash, D. I., Ulrich, T. & Mai, P. M. Rupture dynamics of cascading earthquakes in a multiscale fracture network. *J. Geophys. Res.: Solid Earth* **129**, 2328–2349 (2024).
71. Taufiqurrahman, T. et al. Dynamics, interactions and delays of the 2019 Ridgecrest rupture sequence. *Nature* **618**, 308–315 (2023).
72. Hamling, I. J. et al. Complex multifault rupture during the 2016 Mw 7.8 Kaikōura earthquake, New Zealand. *Science* **356**, eaam7194 (2017).
73. Ulrich, T., Gabriel, A.-A., Ampuero, J.-P. & Xu, W. Dynamic viability of the 2016 Mw 7.8 Kaikōura earthquake cascade on weak crustal faults. *Nat. Commun.* **10**, 1213 (2019).
74. van Dinther, Y., Mai, P. M., Dalguer, L. A. & Gerya, T. V. Modeling the seismic cycle in subduction zones: The role and spatio-temporal occurrence of off-megathrust earthquakes. *Geophys. Res. Lett.* **41**, 1194–1201 (2014).
75. van Zelst, I., Wollherr, S., Gabriel, A.-A., Madden, E. H. & van Dinther, Y. Modeling megathrust earthquakes across scales: one-way coupling from geodynamics and seismic cycles to dynamic rupture. *J. Geophys. Res.: Solid Earth* **124**, 11414–11446 (2019).
76. Wirp, S. A. et al. 3d linked subduction, dynamic rupture, tsunami, and inundation modeling: Dynamic effects of supershear and tsunami earthquakes, hypocenter location, and shallow fault slip. *Front. Earth Sci.* **9** (2021).
77. van Zelst, I., Rannabauer, L., Gabriel, A.-A. & van Dinther, Y. Earthquake rupture on multiple splay faults and its effect on tsunamis. *J. Geophys. Res.: Solid Earth* **127**, 11414–11446 (2022).
78. Jourdon, A., Hayek, J. N., May, D. A. & Gabriel, A.-A. Coupling 3D geodynamics and dynamic rupture: Rheology and stress control on strike-slip fault evolution and earthquake dynamics. *J. Geophys. Res.: Solid Earth* **130**, e2025JB031730 (2025).
79. Chemenda, A. I., Cavalie, O., Vergnolle, M., Bouissou, S. & Delouis, B. Numerical model of formation of a 3-D strike-slip fault system. *Comptes Rendus Geosci.* **348**, 61–69 (2016).
80. Le Pourhiet, L., Huet, B. & Traoré, N. Links between long-term and short-term rheology of the lithosphere: Insights from strike-slip fault modelling. *Tectonophysics* **631**, 146–159 (2014).
81. Guillaume, B., Gianni, G. M., Kermarrec, J.-J. & Bock, K. Control of crustal strength, tectonic inheritance, and stretching/shortening rates on crustal deformation and basin reactivation: insights from laboratory models. *Solid Earth* **13**, 1393–1414 (2022).
82. Roy, N., Roy, A., Saha, P. & Mandal, N. On the origin of shear-band network patterns in ductile shear zones. *Proc. Royal Soc. A: Math. Phys. Eng. Sci.* **478**, 20220146 (2022).
83. Mann, P., Grenville, D. & Burke, K. *Neotectonics of a strike-slip restraining bend system, Jamaica*, Vol. 37, 211–226 (Society of Economic Paleontologists and Mineralogists, 1985).
84. Mann, P., DeMets, C. & Wiggins-Grandison, M. *Toward a better understanding of the Late Neogene strike-slip restraining bend in Jamaica: Geodetic, geological, and seismic constraints*, Vol. 290, 239–253 (Geological Society, London, Special Publications, 2007).
85. Demets, C. & Wiggins-Grandison, M. Deformation of Jamaica and motion of the Gonāve microplate from GPS and seismic data. *Geophys. J. Int.* **168**, 362–378 (2007).
86. Domínguez-González, L., Andreani, L., Stanek, K. P. & Gloaguen, R. Geomorpho-tectonic evolution of the Jamaican restraining bend. *Geomorphology* **228**, 320–334 (2015).
87. Symithe, S., Calais, E., de Chabaliere, J. B., Robertson, R. & Higgins, M. Current block motions and strain accumulation on active faults in the Caribbean. *J. Geophys. Res.: Solid Earth* **120**, 3748–3774 (2015).
88. Benford, B., Tikoff, B. & De Mets, C. Interaction of reactivated faults within a restraining bend: Neotectonic deformation of southwest Jamaica. *Lithosphere* **7**, 21–39 (2014).
89. Leroy, S., Mercier de Lépinay, B., Mauffret, A. & Pubellier, M. Structural and tectonic evolution of the eastern Cayman Trough (Caribbean Sea) from seismic reflection data. *AAPG Bull.* **80**, 222–247 (1996).
90. Leroy, S., Mauffret, A., Patriat, P. & Mercier de Lépinay, B. An alternative interpretation of the Cayman trough evolution from a reidentification of magnetic anomalies. *Geophys. J. Int.* **141**, 539–557 (2000).
91. Corbeau, J. et al. How transpressive is the northern Caribbean plate boundary?. *Tectonics* **35**, 1032–1046 (2016).
92. Mitchell, S. F. & Edward, T. C. P. Geology of the Maastrichtian (Upper Cretaceous) succession of the Jerusalem Mountain inlier in western Jamaica. *Caribbean J. Earth Science* **48**, 29–36 (2016).
93. Wright, V., Hornbach, M., Brown, L., McHugh, C. & Mitchell, S. Neotectonics of Southeast Jamaica Derived From Marine Seismic Surveys and Gravity Cores. *Tectonics* **38**, 4010–4026 (2019).
94. Gomez, F. et al. Fragmentation of the Sinai plate indicated by spatial variation in present-day slip rate along the Dead Sea fault system. *Geophys. J. Int.* **221**, 1913–1940 (2020).
95. Reilinger, R. et al. GPS constraints on continental deformation in the Africa-Arabia Eurasia continental collision zone and implications for the dynamics of plate interactions. *J. Geophys. Res.* **111**, B05411 (2006).
96. Viltres, R. et al. Present-day motion of the Arabian Plate. *Tectonics* **41**, e2021TC007013 (2022).
97. Walley, C. D. *The Lebanon passive margin and the evolution of the Levantine Neo-Tethys*, Vol. 186, 407–439 (Publications scientifiques du Museum, 2001).
98. Ghalayini, R., Daniel, J.-M., Homberg, C., Nader, F. H. & Comstock, J. E. Impact of Cenozoic strike-slip tectonics on the evolution of the northern Levant Basin (offshore Lebanon). *Tectonics* **33**, 2121–2142 (2014).
99. Gomez, F. et al. *Strain partitioning of active transpression within the Lebanese restraining bend of the Dead Sea Fault (Lebanon and SW Syria)*, Vol. 290, 285–303 (Geological Society Special Publication, 2007).
100. Nemer, T. S. & Meghraoui, M. A non-active fault within an active restraining bend: The case of the Hasbaya fault, Lebanon. *J. Struct. Geol.* **136**, 104060 (2020).
101. Van Dusen, S. R. & Doser, D. I. Faulting processes of historic (1917–1962) M > 6.0 earthquakes along the North-central Caribbean margin. *Pure Appl. Geophys.* **157**, 719–736 (2000).
102. Wiggins-Grandison, M. D. Preliminary results from the new Jamaica seismograph network. *Seismol. Res. Lett.* **72**, 525–537 (2001).
103. Hadley, D. & Kanamori, H. Seismic structure of the transverse ranges, California. *Geol. Soc. Am. Bull.* **88**, 1469–1478 (1977).
104. Burov, E. Rheology and strength of the lithosphere. *Mar. Pet. Geol.* **28**, 1402–1443 (2011).
105. Rybacki, E. & Dresen, G. Dislocation and diffusion creep of synthetic anorthite aggregates. *J. Geophys. Res.: Solid Earth* **105**, 26017–26036 (2000).
106. Hirth, G. & Kohlstedt, D. L. Rheology of the Upper Mantle and the Hirtle Wedge: A View from the Experimentalists. *Geophys. Monogr.* **138**, 83–105 (2003).
107. Culling, W. E. H. Soil creep and the development of hillside slopes. *J. Geol.* **71**, 127–161 (1963).

108. Jourdon, A., May, D. A., Hayek, J. N. & Gabriel, A.-A. 3D reconstruction of complex fault system from volumetric geodynamic shear zones using medial axis transform. *Geochem. Geophys. Geosyst.* **26**, e2025GC012169 (2025).
109. Jourdon, A., Le Pourhiet, L., May, D. A., Pubellier, M. & Gabriel, A.-A. Models results for article: Lithospheric models supported by the Caribbean and Levant examples help rethink transpression at plate boundaries. *Zenodo* <https://zenodo.org/records/17724420> (2025).
110. Jourdon, A. Geoteqpy v1.1.2. in geochemistry, geophysics, geo-systems. *Zenodo* <https://doi.org/10.5281/zenodo.15242137> (2025).

## Acknowledgements

This work has been supported by Horizon Europe, project ChESEE-2P, grant no. 101093038 (AJ, LLP, AAG). Numerical models were performed with computing HPC and storage resources from GENCI at TGCC, thanks to the grant no. 2024-A160415068 on the supercomputer Joliot Curie SKL/ROME partition (AJ, LLP). AAG acknowledges additional support from Horizon Europe (DT-GEO, grant number 101058129, Geo-INQUIRE, grant number 101058518), the National Science Foundation (NSF grant numbers EAR-2225286, EAR-2121568, OAC-2139536, OAC-2311208), and the National Aeronautics and Space Administration (NASA 80NSSC20K0495). DAM acknowledges financial support from the National Science Foundation through grants EAR-2121568 and OAC-2311208.

## Author contributions

Conceptualization: A.J., L.L.P., D.A.M., A.A.G. Writing: A.J., L.L.P., M.P., D.A.M., A.A.G. Visualization: A.J. Results interpretation: A.J., L.L.P., M.P. Funding acquisition: L.L.P., A.A.G. Methodology: A.J., D.A.M. Software: A.J., D.A.M.

## Competing interests

The authors declare no competing interests.

## Additional information

**Supplementary information** The online version contains supplementary material available at <https://doi.org/10.1038/s41467-025-68051-2>.

**Correspondence** and requests for materials should be addressed to Anthony Jourdon.

**Peer review information** *Nature Communications* thanks Roy Gabrielsen, Michele Cooke, and the other, anonymous reviewer(s) for their contribution to the peer review of this work. A peer review file is available.

**Reprints and permissions information** is available at <http://www.nature.com/reprints>

**Publisher's note** Springer Nature remains neutral with regard to jurisdictional claims in published maps and institutional affiliations.

**Open Access** This article is licensed under a Creative Commons Attribution-NonCommercial-NoDerivatives 4.0 International License, which permits any non-commercial use, sharing, distribution and reproduction in any medium or format, as long as you give appropriate credit to the original author(s) and the source, provide a link to the Creative Commons licence, and indicate if you modified the licensed material. You do not have permission under this licence to share adapted material derived from this article or parts of it. The images or other third party material in this article are included in the article's Creative Commons licence, unless indicated otherwise in a credit line to the material. If material is not included in the article's Creative Commons licence and your intended use is not permitted by statutory regulation or exceeds the permitted use, you will need to obtain permission directly from the copyright holder. To view a copy of this licence, visit <http://creativecommons.org/licenses/by-nc-nd/4.0/>.

© The Author(s) 2026